Evaluating coarse-grained MARTINI force-fields for capturing the ripple phase of lipid membranes

***Pradyumn Sharma*[1,‡], *Rajat Desikan*[1,‡,†], *K. Ganapathy Ayappa*[1,2,*]**

[1]Department of Chemical Engineering, Indian Institute of Science, Bengaluru, India

[2]Centre for BioSystems Science and Engineering, Indian Institute of Science, Bengaluru, India

[‡]Co-first authors

[†]Present address: Certara QSP, Certara UK Limited, Sheffield, UK

*Corresponding author: K. Ganapathy Ayappa; E-mail: ayappa@iisc.ac.in

Manuscript details:

Title: 96 characters with spaces; Abstract: 272 words; Figures: 6; Tables: 2; References: 76; Supplementary figures: 11

Keywords:

Molecular dynamics; multiscale simulations; CHARMM36; MARTINI; lipid membrane; DPPC; tilted ripple phase; gel phase; phase transition

Abstract

Phospholipids, which are an integral component of cell membranes, exhibit a rich variety of lamellar phases modulated by temperature and composition. Molecular dynamics (MD) simulations have greatly enhanced our understanding of phospholipid membranes by capturing experimentally observed phases and phase transitions at molecular resolution. However, the ripple ($P_{\beta'}$) membrane phase, observed as an intermediate phase below the main gel-to-liquid crystalline transition with some lipids, has been challenging to capture with MD simulations, both at all-atom and coarse-grained resolution. Here, we systematically assess the ability of five coarse-grained MARTINI 1,2-dipalmitoyl-sn-glycero-3-phosphocholine (DPPC) lipid force-field (FF) variants, parametrized to reproduce the DPPC gel and fluid phases, for their ability to capture the $P_{\beta'}$ phase. Upon cooling from the fluid phase to below the phase transition temperature with smaller (380-lipid) and larger (> 2200-lipid) MARTINI and all-atom (CHARMM36 FF) DPPC lipid bilayers, we observed that smaller bilayers with both all-atom and MARTINI FFs sampled interdigitated $P_{\beta'}$ and ripple-like states, respectively. However, while all-atom simulations of the larger DPPC membranes exhibited the formation of the $P_{\beta'}$ phase, similar to previous studies, MARTINI membranes did not sample interdigitated ripple-like states at larger system sizes. We then demonstrated that the ripple-like states in smaller MARTINI membranes were kinetically-trapped structures caused by finite size effects rather than being representative of true $P_{\beta'}$ phases. We showed that even a MARTINI FF variant that could capture the tilted $L_{\beta'}$ gel phase, a prerequisite for stabilizing the $P_{\beta'}$ phase, could not capture the rippled phase upon cooling. Our study reveals that the current MARTINI FFs may require specific re-parametrization of the interaction potentials to stabilize lipid interdigitation, a characteristic of the ripple phase.

1 Introduction

Lamellar lipid membranes, composed of two layers of amphiphilic lipids with solvated hydrophilic 'heads' and buried hydrophobic 'tails', exhibit a wide variety of thermotropic phases such as crystalline (L_c), tilted gel ($L_{\beta'}$) or straight gel (L_β), tilted ripple ($P_{\beta'}$), and liquid-crystalline (L_α).[1,2] Lipid bilayers are important constituents of biomembranes which are ubiquitous in living organisms[3], and nanoparticle pharmaceuticals such liposomal drugs[4–6]. Specifically, lipid membrane phases influence: (i) biological processes at the cellular level such as membrane fusion and budding[7], permeation of drugs[8,9], effect of anaesthetics[10], vulnerability to pathogenic toxins[11,12], lipid flip-flop[13,14], neural signalling[15], and the function of membrane proteins[3,7], and (ii) industrial applications such as the design, storage and usage of liposomal drugs[4–6,16], cosmetic formulations[1], and lipid-rich foods[1]. Molecular simulations of membranes at various levels of detail have yielded atomistic insights into the rich phase behaviour of phospholipid membranes while complementing experimental observations[1,17]. All-atom molecular dynamics (MD) simulations have successfully captured the low temperature $L_{\beta'}$ or L_β phases, the liquid ordered and liquid disordered phases, and the main gel-to-fluid ($L_{\beta'}$ to L_α) phase transition in simple lipid bilayers while providing detailed insights into the rate-limiting formation of the melting seed that nucleates the transition[18]. Similarly, the molecular structure of lipid domains in the elusive $P_{\beta'}$ phase, which commonly occurs upon cooling membranes from the L_α phase to below the gel-to-fluid transition temperature (pre-transition region), and challenging to decipher at atomistic resolution through experiments, was unravelled via detailed MD simulations[19–21], consistent with observations.

While these *in silico* studies illustrate the wide applicability of all-atom lipid force-fields (FFs), all-atom MD simulations are typically limited by computational bottlenecks to nanoscales, and complex membrane processes typically require microscale MD simulations[17,22]. Therefore, coarse-grained (CG) lipid models such as those used in the dissipative particle dynamics (DPD), MARTINI, and other variants have been developed[22–26]. Among the CG models, the MARTINI

68 framework has been successfully used to study a variety of complex biological systems outside
69 the purview of all-atom MD simulations[22]. For example, MARTINI simulations have been used to
70 carry out microsecond simulations of an idealized 20000-lipid plasma membrane comprising 63
71 different species of lipids[27], a difficult feat with typical all-atom simulations. The versatility and
72 computational tractability of CG models such as MARTINI render them as attractive options for
73 capturing the microscopic details of complex membrane phenomena[22,24]. However, since CG
74 models by definition possess reduced molecular detail[28], their interaction potentials must be
75 continuously assessed and refined, often by systematic comparison with corresponding detailed
76 all-atom models[25,26,28–31], to enable increasingly accurate CGMD simulations.

77 DPPC possesses a large headgroup and favourable inter-head interactions that stabilizes
78 a tilted gel ($L_{\beta'}$) phase at lower temperatures, unlike lipids with smaller headgroups such as
79 phosphatidylethanolamine that favour the straight gel (L_{β}) phase[20,21,32]. At higher temperatures,
80 DPPC exhibits a main $L_{\beta'}$ to L_{α} phase transition, with the $P_{\beta'}$ phase occurring at pre-transition
81 temperatures[32–38]. The $P_{\beta'}$ phase has interesting properties such as the influence of thermal
82 history on the symmetry of the ripple domains[20], and therefore has been the subject of extensive
83 experimental[33,37–40] and theoretical[18–21,25,30,35,36,41–45] studies. In Table 1, we summarize some of
84 the previous studies where the rippled phase has been observed, including details of lipid type,
85 resolution (all-atom, united atom or coarse-grained) and FF. Despite extensive *in silico*
86 investigations, MD simulations that capture the $P_{\beta'}$ phase have proven to be challenging since
87 the ripple domain structure and formation is not only a function of the specific lipid FF (Table 1),
88 but also depends on the cooling/heating protocols[18,34] and system size effects[20,34,43]. In spite of
89 these challenges, MD simulations of lipid bilayers in the ripple phase have revealed elusive details
90 of molecular organization that were challenging to probe via experiments, such as the asymmetric
91 sawtooth-like molecular organization of lipids in the DPPC ripple domains[19–21].

92 **Table 1. List of previous studies which have explored the $P_{\beta'}$ phase using MD simulations.**

Lipid	*Year*	*Resolution*	*Force-field*	*Comparison with experiments*	*Citation*
DPPC	2005	United atom	Modified Berger lipid	Qualitative comparison with DMPC electron density profiles	Ref.[19]
DMPC	2005	Coarse-grained	DPD	–	Ref.[21]
DPPC	2007	Coarse-grained	Custom (single tailed)	Qualitative comparison with DPPC electron density maps	Ref.[20]
DMPC, DPPC	2012	Coarse-grained	DPD, MARTINI	Enthalpic signatures of phase transitions from MD compared with differential scanning calorimetry	Ref.[34]
BTMAC+SA	2014	United atom	GROMOS 87, OPLS	–	Ref.[41]
DPPC	2014	Coarse-grained	MARTINI	–	Ref.[46]
DMPC	2016	All-atom	CHARMM36, Lipid14	–	Ref.[42]
DPPC	2017	Coarse-grained	Dry MARTINI	–	Ref.[47]
DMPC, DPPC	2018	All-atom	CHARMM36	Comparison of bilayer properties with X-ray diffraction experiments	Ref.[44]
DPPC	2018	All-atom	CHARMM36	–	Ref.[18]
DPPC	2018	All-atom, coarse-grained	CHARMM36, MARTINI	–	Ref.[30]
DPPC	2019	All-atom	CHARMM36	–	Ref.[43]
BTMAC+SA	2020	All-atom, coarse-grained	CHARMM36, MARTINI	–	Ref.[25]

93 Abbreviations: DPD – dissipative particle dynamics; DPPC – 1,2-dipalmitoyl-sn-glycero-3-phosphocholine; DMPC –
94 1,2-dimyristoyl-sn-glycero-3-phosphocholine; BTMAC – benzyltrimethylammonium chloride; SA – stearyl alcohol.

95 While DPPC membranes described by the standard MARTINI FF and its variants have
96 been shown to capture the gel and fluid states[22,30], there are conflicting reports of their ability to
97 capture the ripple phase. Some MARTINI studies have reported ripple formation both with and
98 without enhanced sampling[30,46,47], while others have reported that MARTINI membranes cannot
99 capture the ripple phase[34], with the interdigitated ripple-like domains observed upon quasi-static
100 cooling from the L_α phase reported to be artefacts caused by finite size effects[34]. Therefore, the
101 ability of MARTINI membranes to capture the $P_{\beta'}$ phase still remains an unresolved problem. To
102 systematically address this issue, we assess the ability of commonly employed[18,19,23,29,30,34,43,44,46]

DPPC bilayers, described by five MARTINI lipid FF variants (described subsequently), to capture the interdigitated tilted ripple membrane phase ($P_{\beta'}$).

We first establish a standard simulated-annealing-based cooling MD protocol, built on previous studies[18–20,30,43,44], that consistently yielded a ripple phase upon cooling from the fluid phase to below the gel-to-fluid phase transition temperature with all-atom DPPC membranes across multiple simulation replicates. By employing the same protocol with MARTINI DPPC membranes, and by fixing other important variables such as initial configurations (L_α phase), system sizes and cooling rates, we checked whether the MARTINI membranes yielded stable ripple phase structures, similar to those observed in all-atom simulations. Five popular MARTINI lipid and water FF combinations were tested: (1) standard MARTINI version 2.2 lipid FF with normal ('MARTINI2n') or polarizable[48] ('MARTINI2p') water, (2) optimized MARTINI FF for DPPC – has refined bond parameters for better reproduction of DPPC membrane phase behaviour and can capture the tilted $L_{\beta'}$ gel phase – with either normal ('MARTINI2On') or polarizable ('MARTINI2Op') water, and, (3) MARTINI 3 beta (version 3.0.b.3.2) with its in-built water model ('MARTINI3b'). For each FF variant, 10 independent replicates of simulated cooling were performed, ensuring sufficient sampling for robust statistical estimates[18,49]. We observed that smaller (380-lipid) MARTINI DPPC bilayers sampled interdigitated ripple-like states that were not observed with larger DPPC membranes (> 2200-lipid). The ripple-like states in these smaller MARTINI DPPC membranes were demonstrated to be kinetically-trapped structures caused due to finite size effects, rather than being representative of a true ripple phase. However, all-atom simulations of both the smaller and larger DPPC membranes exhibited the formation of the $P_{\beta'}$ phase, similar to previous studies. Our observations thus assess the ability of MARTINI lipid FFs to capture the ripple phase and serve as a guide for future CG lipid FF development.

126 ## 2 Methods

127 ### *2.1 All-atom MD simulations of DPPC membranes*

128 The MD protocols employed in this study for simulating DPPC membranes in the gel, ripple
129 and fluid phases are briefly described below. All the simulations performed in this study are
130 summarized in Table 2.

131 For the small membrane atomistic simulations, two charge-neutral, solvated, fluid phase
132 (L_α), 368-lipid membrane configurations at 350 K, with similar spatial coordinates but different
133 starting velocities, were set up using CHARMM-GUI[50–52] as independent replicates (Figs. 1 and
134 S1). The size of the lipid patches was approximately 15.2 nm (x-axis) x 7.6 nm (y-axis) x 9.4 nm
135 (z-axis), with the characteristic dimension of the simulation box in the membrane plane in the
136 range of the periodicity of 12-16 nm corresponding to previously observed ripple profiles in DPPC
137 membranes[19,53]. This was important because the quality of the observed ripples was found to
138 depend on the characteristic box dimension along the ripple formation[20]. Systems whose
139 characteristic box length in the membrane plane were non-integer multiples of ripple periodicity
140 resulted in frustrated and interconnected structures, unlike the clean ripples observed in systems
141 with integer multiple box lengths[20]. Each system contained >10^5 atoms. The water:lipid ratio was
142 set at 50:1, ensuring sufficient hydration normal to the membrane plane (z), so that the systems
143 could be approximated as isolated lipid bilayers along the z-axis.

144 Atomistic simulations were performed using the CHARMM36 FF[42,54,55] implementation
145 (March 2019 version from http://mackerell.umaryland.edu/charmm_ff.shtml) in Gromacs (version
146 2018.6)[56], according to the currently advocated best practices for lipid bilayer simulations[17,57–59].
147 (See Refs.[42,60] for a brief discussion of all-atom and united atom lipid FFs.) A leapfrog integrator
148 (2 fs integration time step) was used along with Verlet buffered lists and three-dimensional
149 periodic boundary conditions. Electrostatic interactions were computed with the particle mesh
150 Ewald algorithm[61], and van der Waal interactions were smoothly switched to zero between 1.0 to

151 1.2 nm. Covalent bonds involving hydrogen atoms were constrained using the LINCS algorithm[62].
152 Simulations were performed in the NPT ensemble with semi-isotropic pressure coupling along
153 the lateral bilayer plane, by employing the stochastic velocity-rescaling thermostat[63] for
154 temperature control, and the Parrinello-Rahman barostat[64] for pressure control, with coupling
155 constants of 0.1 and 2.0 ps, respectively. After energy minimization and equilibration (100 ns) of
156 the initial configurations in the L_α phase (350 K) according to standard CHARMM-GUI protocols[51],
157 the systemic temperatures of the replicates were continuously reduced from 350 K to 290 K at
158 the rate of 1 K per 6 ns, or -0.167 K/ns, by employing the stochastic simulated annealing MD
159 (SAMD) algorithm implemented in Gromacs[56] (360 ns per SAMD replicate). We chose to cool
160 slightly beyond the pre-transition temperature of 300-310 K at which the $P_{\beta'}$ phase is typically
161 observed[18,32,34–36], because super-cooling is often required in kinetic MD simulations for eliciting
162 a phase transition[18,65,66]. The resulting cooled bilayers at 290 K were further equilibrated at a
163 constant temperature of 290 K for 200 ns for thermal and structural stability.

164 To test for finite size effects and to compare with MARTINI simulations (described next),
165 two large 2208-lipid membranes measuring 47.0 nm x 15.7 nm x 15.0 nm and possessing a high
166 water:lipid ratio of 128:1 (>10^6 atoms total; Table 2) were equilibrated in the L_α phase at 350 K.
167 Subsequently, both replicates were cooled to 290 K at the rate of -0.167 K/ns (chosen based on
168 Ref.[18]) and then equilibrated at 290 K for an additional 200 ns.

169

170 ***2.2 MARTINI simulations of DPPC membranes***

171 380-lipid MARTINI DPPC membranes of size 15 nm x 7.5 nm x 10 nm were prepared using
172 the 'INSANE' python module[67]. The water-bead:lipid ratio was ~13.3:1. Since each water bead is
173 equivalent to 4 water molecules, this corresponds to a water:lipid ratio of ~53:1, similar to the
174 small all-atom membranes. As described in the Introduction, five MARTINI FF variants were used:
175 MARTINI2n, MARTINI2p, MARTINI2On, MARTINI2Op and MARTINI3b. MARTINI2n and

176 MARTINI2On systems also contained anti-freeze solvent beads to prevent artefactual freezing of
177 MARTINI water beads.

178 Input CGMD parameters were fixed based on previously reported parameter settings for
179 improved performance[68]. All CGMD simulations were performed with a 20 fs timestep in the NPT
180 ensemble by employing the stochastic velocity-rescaling thermostat[63] (coupling constant of 1.0
181 ps) and the Parrinello-Rahman semi-isotropic barostat[64] (coupling constant of 12.0 ps).
182 Electrostatics were treated with the reaction-field algorithm[69] with a cut-off of 1.1 nm, relative
183 dielectric constant of 2.5 and 15 for systems with and without polarizable water, respectively, and
184 the relative dielectric constant of the reaction field set to infinity. The van der Waal forces were
185 computed with a cut-off of 1.1 nm. Post energy minimization, five CGMD membranes, each
186 described by a MARTINI FF, were equilibrated in the L_α phase at 350 K for 100 ns, followed by
187 simulated cooling from 350 K to 280 K at -0.167 K/ns (420 ns per SAMD replicate). For each FF,
188 10 independent SAMD replicates were simulated for ensuring robustness of observations[49],
189 resulting in a total of 50 CG-SAMD simulations (Figs. 2, S2-S6). The replicates which yielded
190 ripple-like phases were further equilibrated for 1-5 μs at 280 K to ensure that the ripples had
191 attained thermal and structural equilibrium (Fig. 2).

192 To test for finite-size effects, many large MARTINI DPPC bilayer configurations, with both
193 rectangular and square geometries, were constructed and simulated (Table 2).

194

195 **Table 2. Summary of all-atom and MARTINI simulations performed in this study.**

Forcefield	*Time (μs)#*	*Number of replicas*	*System size (L_x x L_y x L_z nm^3)*	*Number of lipids*	*Number of particles*	*Type of MD simulation[a]*	*Temp. (K)*	*Figures*
Small membrane simulations								
CHARMM36	0.10	1	15.7 x 7.8 x 8.4	368	103040	EQMD[&]	350	1, S1
CHARMM36	0.36	2	13.4 x 6.7 x 10.6	368	103040	SAMD	350-290	
CHARMM36	0.20	2	13.4 x 6.7 x 10.6	368	103040	EQMD	290	
MARTINI2n	0.10	1	15.8 x 7.9 x 9.6	380	9626	EQMD[&]	350	2
MARTINI2On	0.10	1	15.8 x 7.9 x 9.6	380	9620	EQMD[&]	350	-
MARTINI3b	0.10	1	15.9 x 7.9 x 9.1	380	9626	EQMD[&]	350	-

MARTINI2p	0.10	1	16.0 x 8.0 x 9.0	380	19761	EQMD[&]	350	-
MARTINI2Op	0.10	1	15.5 x 7.8 x 9.5	380	19764	EQMD[&]	350	-
MARTINI2n	0.42	10	14.2 x 7.1 x 11.1	380	9626	SAMD	350-280	S2
MARTINI2On	0.42	10	13.9 x 7.0 x 11.5	380	9620	SAMD	350-280	S3
MARTINI3b	0.42	10	14.2 x 7.1 x 10.5	380	9626	SAMD	350-280	S4
MARTINI2p	0.42	10	14.4 x 7.2 x 10.2	380	19761	SAMD	350-280	S5
MARTINI2Op	0.42	10	13.8 x 6.9 x 10.9	380	19764	SAMD	350-280	S6
MARTINI2n	5	2[b]	14.3 x 7.1 x 11.0	380	9626	EQMD	280	2, 6
MARTINI2On	5	3[c]	13.9 x 7.0 x 11.4	380	9620	EQMD	280	2, 6, S11
MARTINI3b	5	1[d]	14.0 x 7.0 x 10.7	380	9626	EQMD	280	2
MARTINI2p	5	1[e]	14.3 x 7.2 x 10.2	380	19761	EQMD	280	2
MARTINI2Op	5	1[f]	13.8 x 6.9 x 10.9	380	19764	EQMD	280	2
Large membrane simulations								
CHARMM36	0.02	1	46.4 x 15.4 x 16.1	2208	1135872	EQMD[&]	350	3, S7
CHARMM36	0.36	2	40.3 x 13.4 x 19.9	2208	1135872	SAMD	350-290	
CHARMM36	0.20	2	40.4 x 13.5 x 19.8	2208	1135872	EQMD	290	
MARTINI2n	0.10	2	46.5 x 15.5 x 20.6	2204	112719	EQMD[&]	350	4
MARTINI2On	0.10	2	46.3 x 15.4 x 20.8	2204	112719	EQMD[&]	350	-
MARTINI3b	0.10	2	47.1 x 15.7 x 18.8	2204	112717	EQMD[&]	350	-
MARTINI2n	0.42	2	39.9 x 13.3 x 26.0	2204	112719	SAMD	350-280	4, S9*a*
MARTINI2On	0.42	2	39.9 x 13.1 x 26.6	2204	112719	SAMD	350-280	
MARTINI3b	0.42	2	41.3 x 13.8 x 22.7	2204	112717	SAMD	350-280	
MARTINI2n	3	1	39.6 x 13.2 x 12.7	2280	57756	EQMD	280	5, S10
MARTINI2On	5, 8, 10	3	39.7 x 13.2 x 12.6	2280	57720	EQMD	280	5, 6, S10, S11
MARTINI3b	10	1	40.0 x 13.3 x 11.8	2280	57756	EQMD	280	5, S10
MARTINI2On	0.10	1[g]	46.5 x 46.5 x 20.2	6728	333604	EQMD[&]	350	-
MARTINI2On	0.42	2[g]	39.5 x 39.5 x 26.0	6728	333604	SAMD	350-280	S9*b*

[#]Simulation times from MARTINI CGMD were not scaled. Total simulation time in this study: ~2.5 μs (all-atom MD) and ~87 μs (MARTINI CGMD). [&]Initial simulations to equilibrate starting configurations. [a]EQMD – equilibrium MD simulations in the NPT ensemble; SAMD – simulated annealing MD simulations at constant pressure. [b]Replicates with the 'best' ripple-like (Repl. 1 in Fig. S2) and straight gel (Repl. 7 in Fig. S2) phases were further equilibrated for 5000 ns. [c]Replicates with the 'best' ripple-like (Repl. 5 in Fig. S3), tilted ripple-like (Repl. 7 in Fig. S3) and tilted gel (Repl. 3 in Fig. S3) phases were further equilibrated for 5000 ns. [d]Replicate with the 'best' ripple-like phase (Repl. 9 in Fig. S4) was further equilibrated for 5000 ns. [e]Replicate with the 'best' ripple-like phase (Repl. 5 in Fig. S5) was further equilibrated for 5000 ns. [f]Replicate with the 'best' ripple-like phase (Repl. 10 in Fig. S6) was further equilibrated for 5000 ns. [g]Square membrane patch; all others are rectangular membrane patches

2.3 Analysis and visualization

MD snapshots are illustrated using the visual molecular dynamics 1.9.3 (VMD)[70] software. The DPPC tails in the upper and lower leaflets of both all-atom and MARTINI membranes are consistently colored cyan and magenta, respectively. In all-atom membranes, phosphorus atoms

(P) are colored orange, and nitrogen atoms in the choline group are colored blue. Similarly, in MARTINI membranes, the phosphate bead is colored orange and the choline bead is colored blue. The minimum inter-leaflet P-P distance (ξ), which is an order parameter to track leaflet interdigitation (Fig. 1*b*), was computed using the inbuilt 'gmx mindist' tool in Gromacs. The ξ from the fluid and interdigitated regimes are fit to a four-parameter piecewise-linear function (Eq. 1) to accurately estimate the time of the onset of membrane interdigitation, τ.

$$\xi = (m_1 t + c)\big(1 - H(t-\tau)\big) + (m_2 t + (m_1 - m_2)\tau + c)H(t-\tau) \qquad -(1)$$

Here, m_1 and m_2 are the slopes of the two lines corresponding to the fluid and interdigitated regimes (when it occurs), respectively, c is the intercept of the fluid-phase line (the intercept of the other line is $(m_1 - m_2)\tau + c$ from the point of intersection), and $H(t-\tau)$ is the Heaviside function which is zero for $t < \tau$, and one for $t \geq \tau$. If interdigitation occurs, $m_2 < 0$, else $m_2 > 0$ (illustrated in Fig. S2). The fitting was performed using the 'lsqcurvefit' function (optimization toolbox) in conjunction with 'multistart' (global optimization toolbox) implemented in MATLAB 2018a (https://www.mathworks.com). All other plots are also created with MATLAB. The combined Voronoi-thickness modulation heatmaps are plotted using the 'voronoi' MATLAB function on the lipid phosphorus atom x, y coordinates (upper leaflet) from the corresponding MD snapshot. The membrane thickness[41] is computed using the 'Membplugin' 1.1 tool[71] in VMD and visualized using MATLAB. Similar to a previous study[72], lipid tilt angles from MARTINI membranes (L_β vs. $L_{\beta'}$) were computed from the last 10 ns of the respective MD trajectories, using the inbuilt 'gmx gangle' tool in Gromacs. The lipid tilt was defined as the angle between the lipid vector and the leaflet normal, with the lipid vector defined as the vector joining the center of mass of the terminal tail beads with the head phosphate bead.

3 Results and Discussion

3.1 Ripple formation in atomistic simulations of DPPC membranes

To robustly capture the ripple phase in all-atom DPPC membranes[26], well-equilibrated, fluid, 368-lipid DPPC membranes at 350 K (time point I in Fig. 1*a, c*) were cooled to 290 K, lower than the experimentally observed pre-transition temperature of 300-310 K[32,34–36] and sufficient to ensure leaflet interdigitation[18,44], using the stochastic simulated annealing MD algorithm, followed by constant temperature equilibration MD (EQMD) in the NPT ensemble at 290 K to ensure thermal equilibration and structural convergence (details in Methods; 2 independent MD replicates). Along with the initial state (time point I), three other time points are important in the combined SAMD+EQMD trajectory (Fig. 1*a, c*) – the fluid membrane configuration where interdigitation starts (time point II), the fully interdigitated ripple phase membranes at the end of simulated cooling (time point III), and the converged systems at the end of constant temperature equilibration (time point IV). The extent of interdigitation was tracked by the minimum inter-leaflet P-P distance with time (ξ; Methods and Eq. 1; Fig. 1*b, c*). A higher initial value marked the baseline corresponding to the fluid phase (350 K; time point I), and an abruptly decreasing trend indicated significant interdigitation of lipids from opposite leaflets, with the onset of interdigitation marked by the inflection point (time point II – τ; see Methods, Fig. S2, and Eq. 1). By the end of simulated cooling (290 K; time point III), interdigitation was complete and a membrane with an 'asymmetric'[20] 1D ripple was formed, similar in structure to previous studies[19,20,43,44], structurally stable upon further 200 ns equilibration at 290 K (time point IV), and with clearly distinct major and minor arms (illustrated in Fig. S1*a*).

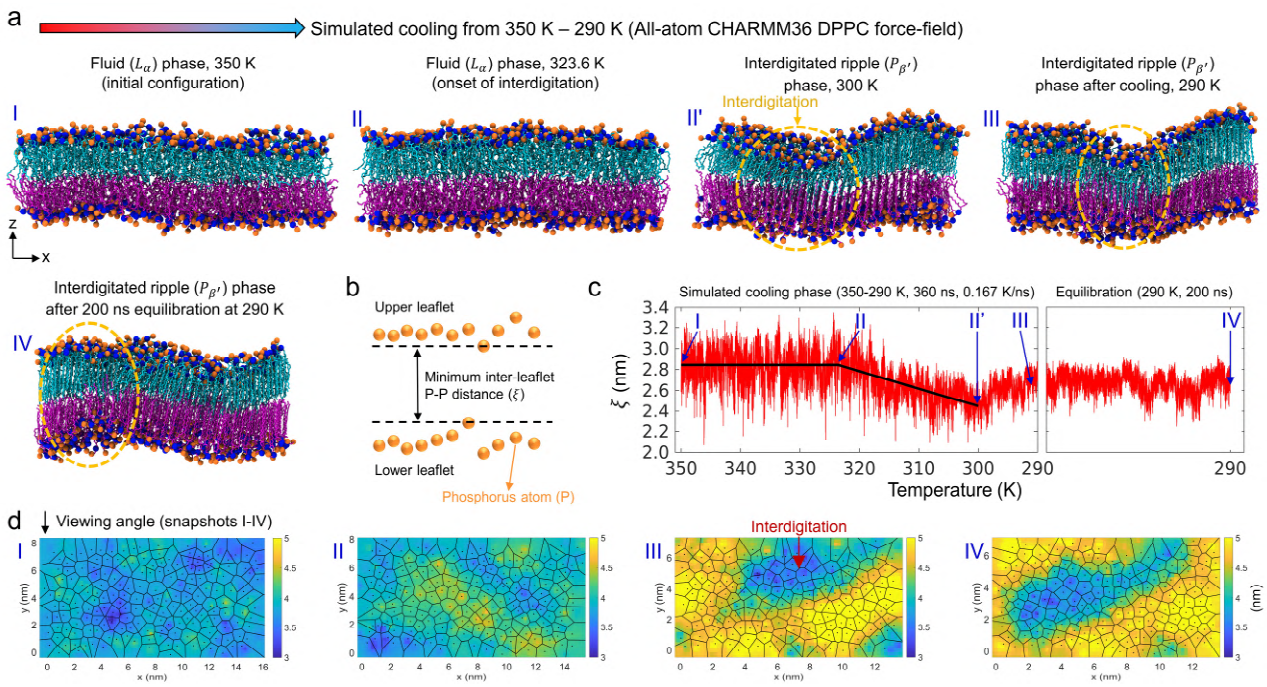

Fig. 1. All-atom L_α DPPC membranes consistently form ripples upon cooling. (a) MD snapshots (colouring described in Methods) during the cooling of a 368-lipid, all-atom, DPPC membrane from 350 K to 290 K. Time points: I – initial equilibrated L_α phase membrane at 350 K before the start of cooling, II – start of interdigitation, II' –time at which the average inter-leaflet distance in the time series is at a minimum (300 K), III – end of simulated cooling (290 K), and IV – end of equilibration MD at constant temperature (290 K). Interdigitated domains are highlighted by yellow dashed circles. **(b)** Schematic illustrating the minimum inter-leaflet P-P distance, ξ, which is used as an order parameter to track leaflet interdigitation (Eq. 1). **(c)** Time trace (red) and biphasic linear fits (black) of ξ in cooling simulations of atomistic DPPC membranes. **(d)** Voronoi diagram from the x-y coordinates of the upper leaflet P atoms depicting the area per head group of individual lipids is superimposed on the thickness modulations of membranes at time points I-IV, corresponding to the MD snapshots in (a) (viewing angle pictorially depicted).

Voronoi-thickness membrane maps, which are Voronoi diagrams of the upper membrane leaflet superimposed onto P-P thickness heatmaps[25,41], are shown in Fig. 1*d*, corresponding to the top views of MD snapshots in Fig. 1*a*. The trends were similar[41] when the Voronoi diagrams were plotted using the lower leaflets (not shown). Compared to the uniform topography in the fluid phase, the formation of interdigitated (blue) and gel (yellow) domains in the ripple phase can be clearly observed. There is negligible difference in membrane topographies between time points III and IV except for the lateral movement of membrane across period boundaries, indicating that

274 the ripple phase membrane configuration at the end of simulated cooling is at equilibrium. An
275 interesting observation was that the interdigitated ripple domain (Fig. 1*d*) appeared to be tilted in
276 the lateral plane, whereas ripple domains in previous studies[19,20,41] were typically parallel to one
277 of the lateral box edges. Previous mesoscopic lipid bilayer simulations[21] have revealed that at the
278 highest value of the lipid head-head repulsion parameter explored, lower and higher values of
279 which either abrogated or stabilized the ripple phase, respectively, the bilayer formed a laterally
280 tilted ripple domain and a stable $P_{\beta'}$ membrane phase similar to our observations.

281 Another independent all-atom MD replicate also yielded a similar interdigitated DPPC
282 ripple phase membrane upon cooling (Fig. S1*b*), thus validating the robustness of the above MD
283 protocol to produce the $P_{\beta'}$ phase from fluid membrane configurations. We next employed this
284 MD cooling protocol to fluid-phase MARTINI membranes (all five FF variants) and evaluated their
285 ability to capture the ripple phase.

286

287 ***3.2 Ripple formation in smaller MARTINI membranes***

288 Fluid phase, 380-lipid, DPPC MARTINI membranes belonging to five MARTINI FF variants
289 were cooled from 350 K to 280 K, and evaluated for their ability to form the interdigitated $P_{\beta'}$
290 membrane phase (see Introduction and Methods). The lower bound for temperature was set to
291 280 K, compared to 290 K for all-atom, because a previous CGMD study showed that ripple-like
292 interdigitated phases in MARTINI DPPC membranes were formed between 280-290 K[34]. The
293 trajectory of an SAMD+EQMD replicate with the MARTINI2n FF is shown with time points I-IV
294 highlighted (Fig. 2*a*-*c*). The constant temperature EQMD phase post cooling was chosen to be 5
295 μs for MARTINI (Fig. 2*b*), compared to 200 ns for the all-atom simulations (Fig. 1*c*). Similar to the
296 time course seen in atomistic DPPC membranes, a majority (70%), but notably not all,
297 MARTINI2n replicates showed interdigitation of membrane leaflets (time points I-IV on the $\xi(t)$
298 plot, Voronoi-thickness maps pertaining to MD snapshots at time points I and IV), thus apparently

299 capturing ripple-like membrane states. This is in accord with previous single replicate studies,
300 where MARTINI membranes of similar sizes captured the ripple phase[30,34,46,47]. In the rest of the
301 MARTINI2n replicates (30%), the membranes bypassed the interdigitated ripple-like state and
302 directly froze into L_β configurations (Fig. S2). This emphasizes that with simulated cooling MD,
303 rippling in MARTINI membranes depended on the initial configuration and starting velocities, and
304 therefore necessitated multiple MD replicates for obtaining robust trends.[49]

305 The orientation of the interdigitated domains in the MARTINI2n membranes were
306 perpendicular to the x-axis (Fig. 2*c*) in contrast with the laterally tilted interdigitated domains seen
307 in all-atom simulations (Figs. 1*d* and S1*b*). Similar domains were observed in a previous MARTINI
308 study.[34]

309 Formation of ripple-like phases in DPPC membranes described by the other FF variants –
310 MARTINI2On, MARTINI3b, MARTINI2p, and MARTINI2Op – are summarized in Fig. 2*d*-*g* (all MD
311 replicates for each FF variant displayed in Figs. S3-S6, respectively). MARTINI2On is similar to
312 MARTINI2n, with 70% of the replicates forming ripple-like (Figs. 2*d* and S3). MARTINI3b, the beta
313 version of the improved[73] next generation MARTINI3 FF (unpublished and currently under
314 development), showed ripple-like formation in a minority (30%) of the replicates (Figs. 2*e* and S4).
315 The MARTINI FF combinations with polarizable water, MARTINI2p (Figs. 2*f* and S5) and
316 MARTINI2Op (Figs. 2*g* and S6), showed ripple-like states in only 10% and 30% of replicates,
317 respectively, despite the reparameterization of polarizable water to improve the accuracy of
318 solvent electrostatic effects[48], important for capturing macroscopic membrane properties[54,55]. Our
319 observations with MARTINI2p are to be contrasted with previous single-replicate MARTINI[34]
320 simulations, where quasi-static cooling of fluid-phase membranes resulted in the formation of the
321 ripple-like domains only with polarizable water. While differences in MD protocols and differences
322 in the initial configurations may explain the disparities, careful future investigations, with systems
323 of varying size, may be necessary to determine the predictive accuracy of polarizable water-lipid
324 interactions.

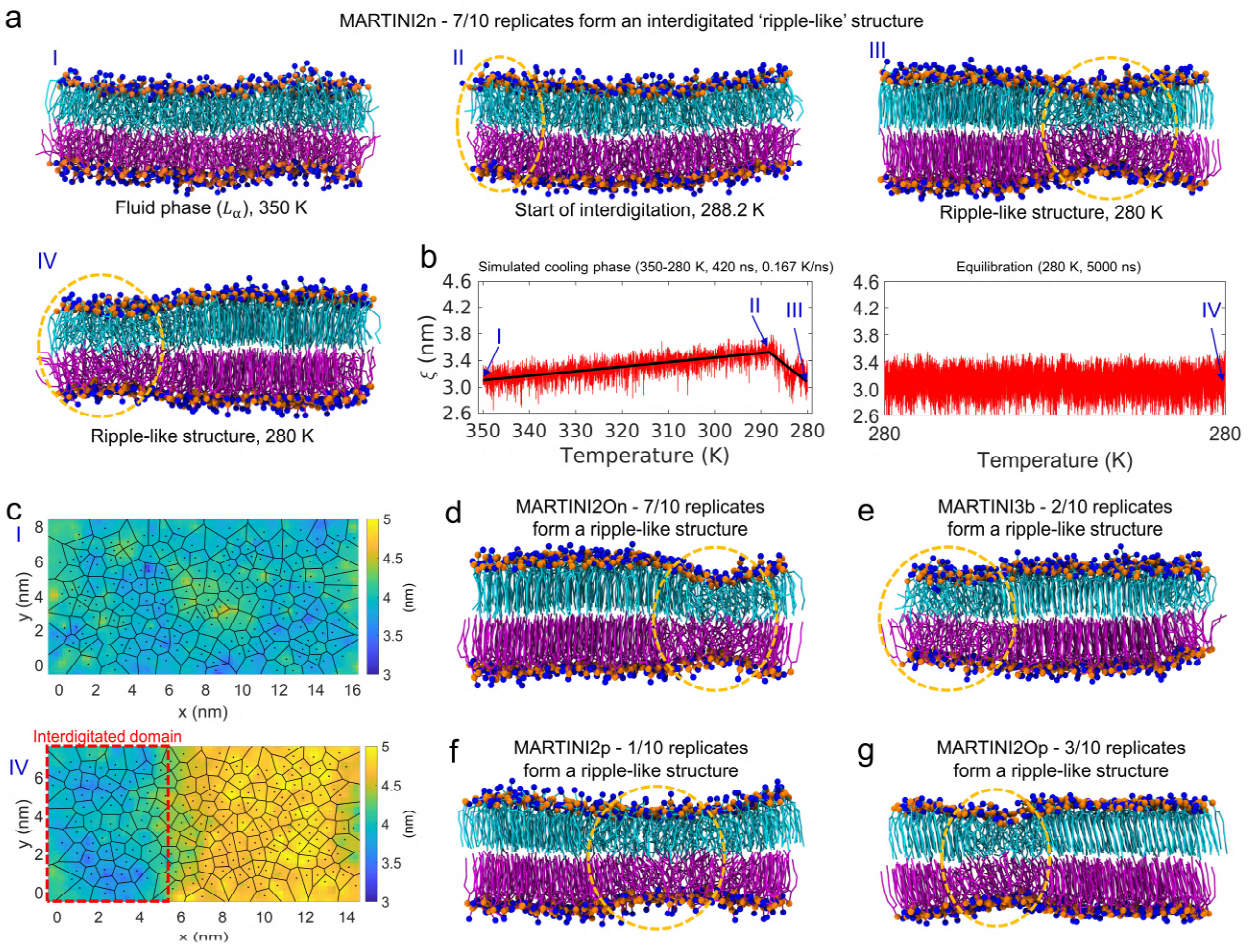

Fig. 2. Smaller MARTINI membranes form a ripple-like interdigitated phase upon cooling. **(a)** Similar to all-atom MD (Fig. 1), snapshots from time points I-IV from the simulated cooling of a MARTINI2n membrane replicate from 350 K – 280 K are shown (Replicate 1 from Fig. S2). Interdigitated regions are highlighted by a yellow dashed circle. **(b)** Minimum inter-leaflet P-P distance with time in the 420 ns cooling and 5000 ns constant temperature equilibration phases. **(c)** Voronoi-thickness maps contrasting the initial fluid membrane and the final interdigitated ripple-like membrane (time points I and IV, respectively). Cooling of 7/10 independent MARTINI2n MD replicates resulted in the formation of a ripple-like phase (Fig. S2). Other MARTINI FF variants: **(d)** MARTINI2On (Replicate 5 from Fig. S3), **(e)** MARTINI3b (Replicate 9 from Fig. S4), **(f)** MARTINI2p (Replicate 5 from Fig. S5) and **(g)** MARTINI2Op (Replicate 10 from Fig. S6), show the formation of ripple-like phases in 7, 2, 1 and 3 out of 10 replicates each, respectively (Figs. S3 – S6). These snapshots correspond to time point IV.

3.3 Testing for ripple formation in large atomistic and MARTINI DPPC membranes upon simulated cooling

342 In a previous study, Rodgers *et al.*[34] observed the interdigitation of lipids in relatively small
343 512-lipid MARTINI DPPC membranes upon quasi-equilibrium, stepwise, simulated cooling of fluid
344 membranes from 325 K to less than 280 K. These small membranes apparently sampled an
345 interdigitated ripple-like phase, similar to our observations (Fig. 2). However, when the exercise
346 was repeated with 4-times-larger (2048-lipid) DPPC membranes, the ripple-like phase could not
347 be reproduced. Thus, Rodgers *et al.*[34] concluded that the interdigitated ripple-like states in smaller
348 membranes were actually 'intermediate' kinetically trapped membrane states rather than a true
349 ripple phase. In contrast to these MARTINI simulations, a large all-atom 3200-lipid DPPC
350 membrane has been shown to form an interdigitated ripple phase[30], albeit with a different MD
351 protocol. Therefore, we next tested ripple formation in large all-atom DPPC membranes with our
352 simulated cooling MD protocol (similar to Fig. 1), that would re-establish a benchmark to test for
353 ripple formation and system size effects in large MARTINI membranes.

354 We set up two 2208-lipid DPPC bilayer configurations, which were 6-times-larger than the smaller
355 atomistic DPPC membranes shown in Fig. 1, and larger than the membranes employed by
356 Rodgers *et al.*[34], and pre-equilibrated them in the L_α phase at 350 K (Fig. 3*a*). Subsequently,
357 these membranes were cooled to 290 K with the same SAMD protocol. One of the all-atom MD
358 replicates in the fluid phase formed an interdigitated ripple phase membrane by 290 K (Fig. 3*b*).
359 The other replicate (Fig. S7) formed a non-interdigitated 'symmetric' ripple[20] in the larger
360 dimension, which is typically observed upon slow cooling from the fluid phase to approximately
361 the gel-to-fluid transition temperature[20], and an asymmetric interdigitated ripple (similar to Figs.
362 1, 3) in the smaller dimension. Therefore, both smaller and larger all-atom DPPC membranes,
363 described by the CHARMM36 FF, sample the thermodynamic ripple phase upon simulated
364 cooling MD without any evidence of finite size artefacts. In contrast to smaller membranes (Figs.
365 1*d* and S8), the Voronoi-thickness map of the first replicate (Figs. 3*b* and S8) shows reticulated
366 ripple domains. Our observations are in accord with previous studies[30,43], where simulated
367 quenching of 1280-lipid and 3200-lipid all-atom DPPC membranes to below the main transition

temperature also resulted in reticulated ripple domains. It is conceivable that significantly longer runs would be required to anneal and reorganize the ripples along a given direction.

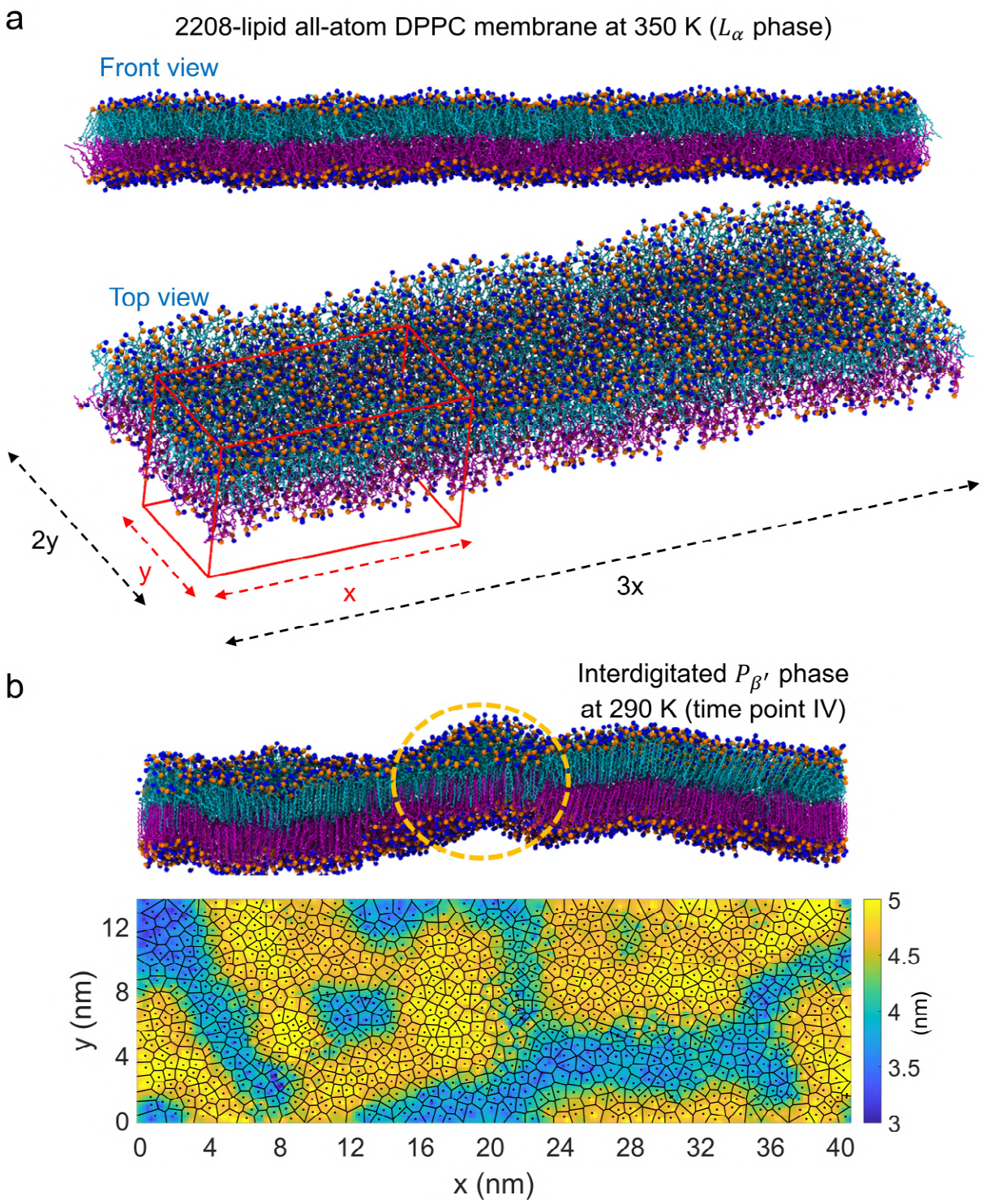

Fig. 3. Ripple formation from all-atom MD of a large DPPC membrane. (a) Front and top views of a large 2208-lipid DPPC membrane which was pre-equilibrated in the fluid phase at 350 K. For comparison, a representative simulation box of a smaller all-atom membrane (Fig. 1) is shown in red. The large membrane is 6-times (3X times 2Y) larger than the smaller membrane. **(b)** Front view of the large membrane after cooling to 290 K and EQMD (corresponds to time point IV), and its Voronoi-thickness modulation map (blue represents interdigitated regions) shows the formation of an aperiodic and reticulated interdigitated ripple domain (also see Figs. S7-S8).

We next tested whether large, fluid, rectangular, 2204-lipid MARTINI DPPC membranes, with normal (not polarizable) MARTINI water, also sampled the interdigitated ripple-like phase upon cooling from 350 K to 280 K. Two initial configurations each for MARTINI2n, MARTINI2On and MARTINI3b FFs were set up analogous to the large all-atom membranes in Fig. 3, and pre-equilibrated at 350 K, followed by cooling to 280 K (Figs. 4 and S9). However, none of the large MARTINI membranes captured a ripple-like phase upon cooling to 280 K. MARTINI2n and MARTINI3b membranes directly froze into the L_β phase, while the MARTINI2On membranes transitioned to the $L_{\beta'}$ phase (Fig. 4b); confirmed by independent MD replicates (Fig. S9*a*). To ensure that membrane geometry did not influence these results, we repeated these simulations with large 6728-lipid square MARTINI2On membranes, and these also did not sample ripple-like states (Fig. S9*b*). Since only smaller (380-lipid) but not larger (>2204-lipid) DPPC MARTINI membranes captured the interdigitated ripple-like states, in contrast to all-atom membranes, we inferred that the smaller MARTINI ripple-like membranes (Figs. 2, S2-S6) represent kinetically-trapped states caused by finite box-size effects rather than true ripple states.

3.4 Equilibrium MD simulations of large MARTINI membranes initialized in the ripple-like phase show loss of interdigitation

To confirm the aforementioned inference, we employed an orthogonal approach where multi-μs equilibrium simulations of large MARTINI membranes, initialized in periodic interdigitated ripple-like configurations, were performed at 280 K. These large systems were created from the

400 final, interdigitated, ripple-like, smaller (380-lipid) MARTINI membrane configurations after 1 μs
401 of constant temperature EQMD at 280 K. The smaller membranes were repeated 6-times along
402 the lateral bilayer plane across periodic boundaries (3x times 2y), and the initial large 2204-lipid
403 ripple-like membrane configurations thus created are displayed in Fig. 5*a, c, d* and correspond to
404 MARTINI2On, MARTINI2n and MARTINI3b, respectively.

405 The rationale behind performing equilibrium MD of these large systems was simply to test
406 if the ripple-like states were stabilized due to finite size effects. Upon 3-10 μs of constant
407 temperature NPT-MD at 280 K, we observed that the large interdigitated MARTINI membranes
408 spontaneously froze into the gel phase, as shown by both MD snapshots (Fig. 5) and Voronoi-
409 thickness maps (Fig. S10), indicating that the initial rippled state configuration was unfavourable
410 at larger system sizes. This phenomenon was observed for all the three MARTINI FF variants,
411 although the time scale over which interdigitation disappeared leading to formation of the final gel
412 phase configuration varied amongst the 3 FFs. MARTINI2On showed progressive loss of
413 interdigitation which was nearly complete by 8 μs (Figs. 5*b* and S10*a*). Longer simulations may
414 have shown a complete loss of interdigitation, but we did not further pursue these computationally
415 intensive MD simulations since the progressive loss of interdigitation with time was apparent (Fig.
416 S10*a*). MARTINI2n showed a rapid and complete loss of interdigitation by 3 μs (Figs. 5*c* and
417 S10*b*), and MARTINI3b showed near-complete loss of interdigitation by 10 μs (Figs. 5*d* and
418 S10*c*), similar to MARTINI2On. In contrast, none of the smaller membranes showed any loss of
419 interdigitation upon 5 μs of constant temperature EQMD at 280 K (Fig. 2).

420 Together with observations from the simulated cooling of large fluid membranes, these two
421 orthogonal MD approaches (Figs. 4 and 5) strongly suggest that MARTINI membranes (all FF
422 variants) do not capture the thermodynamic ripple phase unlike all-atom membranes. Our
423 systematic study implies that ripple-like phase formation observed in smaller MARTINI
424 membranes was due to kinetic trapping of interdigitated leaflets at small system sizes. The few
425 studies which indeed report MARTINI ripple phase membranes, both with[47] and without[34,46]

enhanced sampling, are with smaller membranes composed of 390[47] and 512[34,46] lipids, respectively. Therefore, based on our finding, the formation of rippled bilayers in these studies could be attributed to finite size artefacts[34]. Thus, MARTINI FF parameters may have to be tuned to reproduce the lipid membrane phase diagram, in particular the $P_{\beta'}$ phase, more accurately. FF approaches that tune the bonded parameters of MARTINI lipids based on comparison with all-atom simulations[25,30,34] may result in models that better capture membrane phase behaviour.

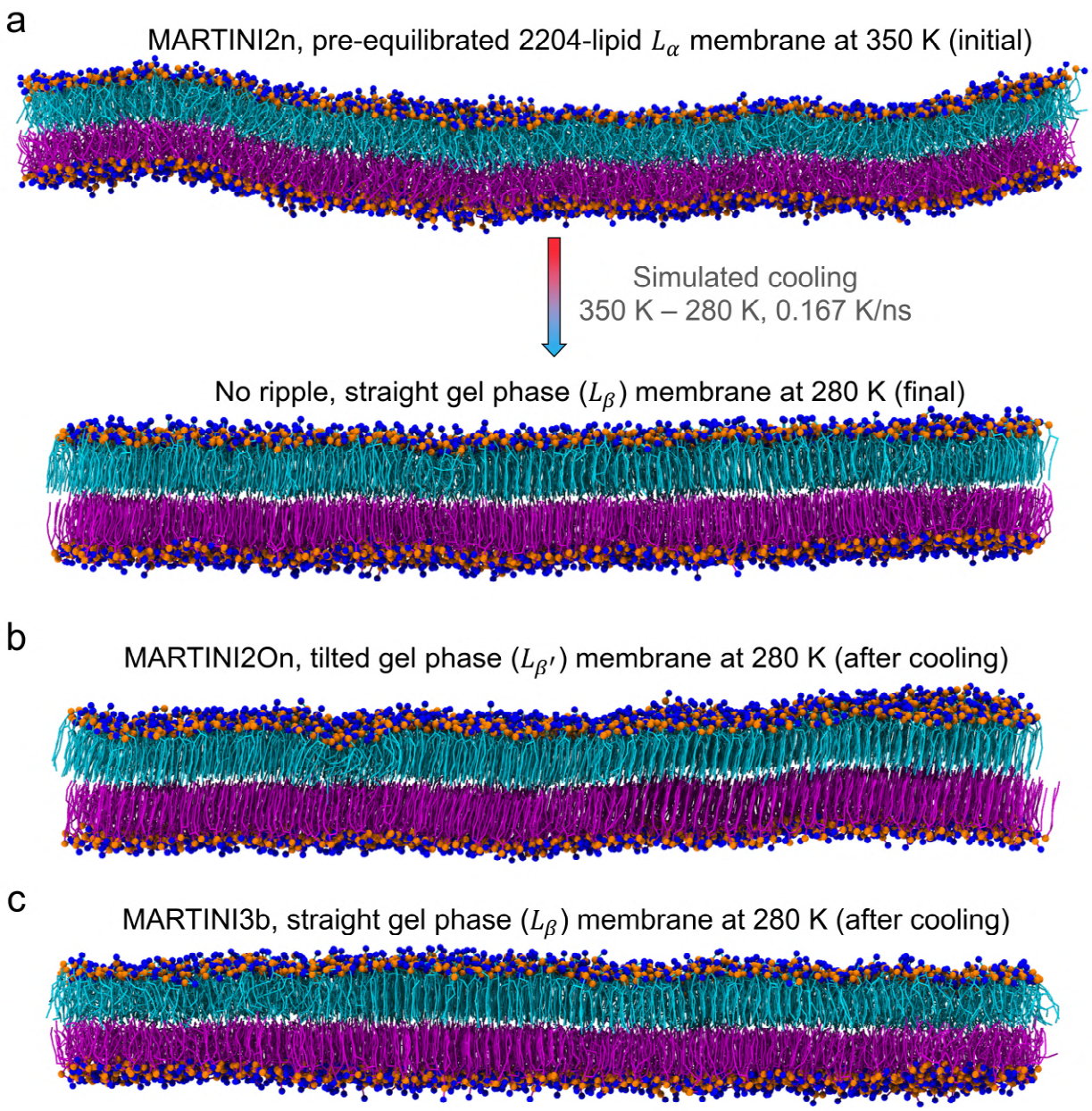

Fig. 4. Lack of ripple formation in large MARTINI DPPC membranes. (a) A representative 2204-lipid, rectangular, MARTINI2n DPPC membrane, pre-equilibrated at 350 K in the L_α phase, was cooled directly into the gel phase at 280 K without the membrane sampling a ripple-like phase, unlike all-atom systems (see Fig. 3). This behaviour was also observed with **(b)** MARTINI2On and **(c)** MARTINI3b FFs. Independent MD replicates are shown in Fig. S9*a*. Two independent simulation replicates, where large 6728-lipid, square, MARTINI2On membranes were cooled to 290 K, also showed a similar lack of sampling of a ripple-like phase (Fig. S9*b*), suggesting that system geometry did not influence our observations.

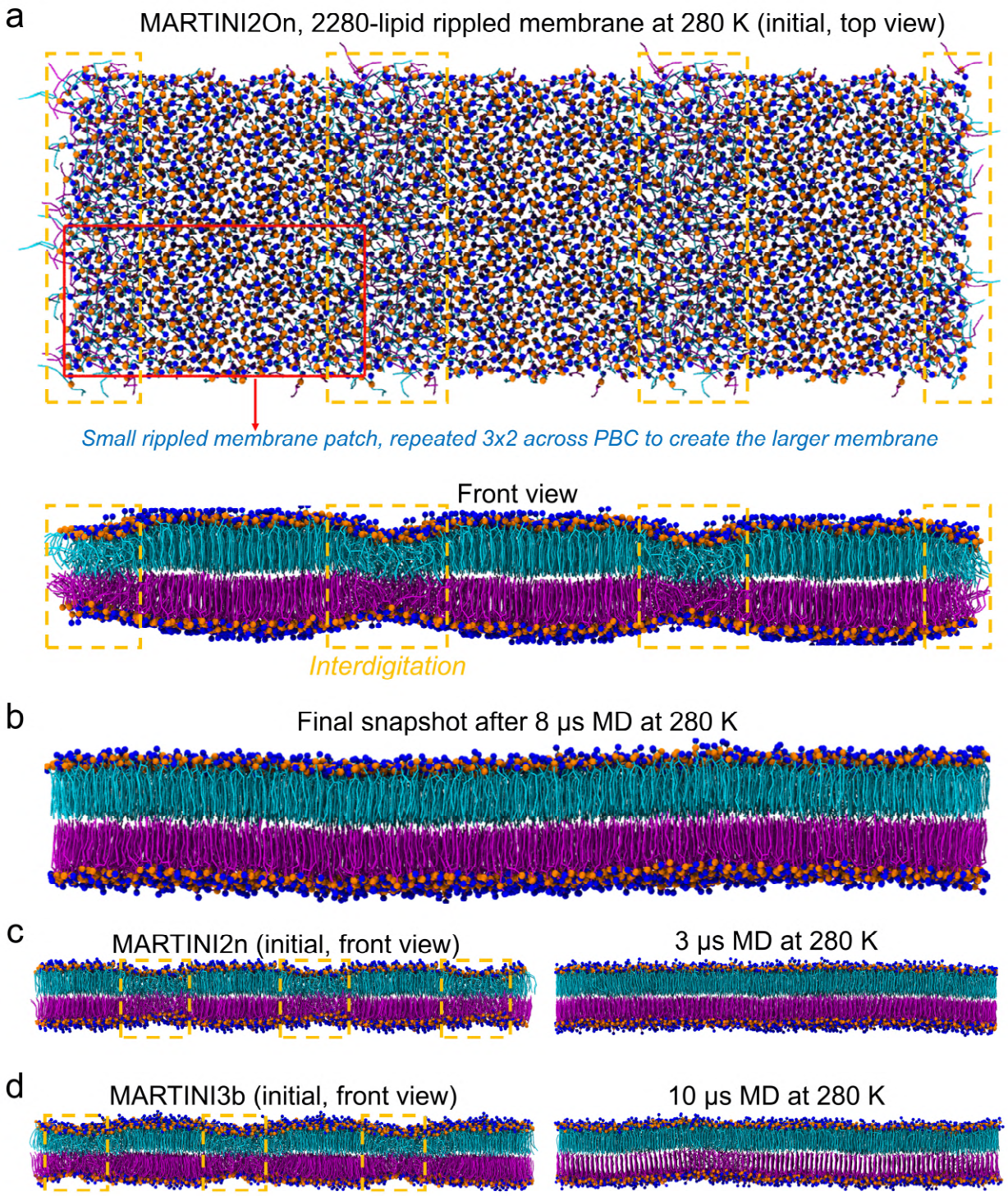

Fig. 5. MD simulations of large MARTINI DPPC membranes starting with interdigitated ripple-like states. (a) To test for spontaneous loss of kinetically trapped domains (yellow dashed rectangles), a larger 2204-lipid MARTINI2On DPPC membrane configuration with periodic ripples (top and front views) was created by repeating smaller rippled membranes (from time point IV, Fig. 2d) six-times across periodic boundary conditions (thrice in X, twice in Y). **(b)** 8 μs MD at 280 K almost completely abolished the interdigitated ripple-like configuration and led to the establishment of the L_β phase (Voronoi-thickness maps in Fig. S10*a*). Similar loss of the ripple-like domains was seen for large MARTINI2n **(c),** and MARTINI3b **(d),** membranes (Voronoi-thickness maps in Fig. S10*b, c*).

3.5 The optimized MARTINI DPPC FF (MARTINI2On) forms the $L_{\beta'}$, but not $P_{\beta'}$, phase

DPPC, with its large headgroup and strong head-head interactions, favours a tilted gel ($L_{\beta'}$) phase at lower temperatures. Therefore, during the L_α → $L_{\beta'}$ transition upon simulated cooling, the tilted ripple ($P_{\beta'}$) state occurs. Lipids exhibiting an L_β state at lower temperatures, such as phosphatidylethanolamines[74], show a single phase transition and do not form the ripple phase[20]. In our small membrane simulations, MARTINI2n (Fig. S2) and MARTINI3b (Fig. S4) froze into L_β states below transition temperatures, in accord with previous studies[34,47]. (MARTINI2n was shown to sample the $L_{\beta'}$ phase only upon enhanced sampling[75].) This may explain to some extent their inability to capture the $P_{\beta'}$ phase. However, MARTINI2On, possessing optimized DPPC bond parameters that closely match macroscopic membrane properties from all-atom simulations, spontaneously captured the $L_{\beta'}$ phase in many of the small membrane replicates upon cooling with classical MD simulations (Fig. S3). This is in agreement with the previous study[30] that developed the MARTINI2On DPPC parameters, where the authors also observed the formation of the $L_{\beta'}$ phase without enhanced sampling. Even in replicates that formed interdigitated ripple-like configurations (Fig. S3), the non-interdigitated gel-like domains often resembled the $L_{\beta'}$ phase.

To further contrast the lipid tilt in the gel phase configurations of DPPC MARTINI2n and MARTINI2On membranes, we chose representative replicates (#7 in Fig. S2, #3 and #7 in Fig. S3) that had frozen into gel states after SAMD without sampling interdigitated ripple-like states,

473 and further equilibrated them at 280 K for 5 μs in the NPT ensemble. The final MD snapshots for
474 MARTINI2n (#7 from Fig. S2) and MARTINI2On (#7 from Fig. S3) are illustrated in Fig. 6*a, b*.
475 Clearly, MARTINI2n and MARTINI2On form stable L_β and $L_{\beta'}$ configurations, respectively, at 280
476 K. For both systems, we quantified the extent of lipid tilt from the tilt angle (θ°) distributions of
477 lipids with their respective leaflet normal (Methods; Fig. 6*c*). The MARTINI2n and MARTINI2On
478 gel phase tilt distributions were observed to have modes at 7.3° and 15.2°, respectively.

479 To ensure that the MARTINI2On $L_{\beta'}$ configuration was not a consequence of finite size
480 artefacts, we created a 6-times-larger membrane by repeating the membrane from Fig. 6*b* across
481 periodic boundaries (3x times 2y; similar to Fig. 5). This initial configuration is shown in Fig. 6*d*,
482 and was simulated at 280 K for 5 μs. From the final snapshot (Fig. 6*d*), the $L_{\beta'}$ configuration is
483 completely preserved. Additionally, simulated cooling of a large L_α MARTINI2On membrane from
484 350 K – 280 K also resulted in a $L_{\beta'}$ configuration (Fig. 4*b*). These observations strongly suggest
485 that MARTINI2On membranes can sample the true $L_{\beta'}$ phase at lower temperatures, without any
486 finite size artefacts, and in agreement with previous studies[30]. However, our multi-replicate
487 simulations show that MARTINI2On membranes also stochastically sample the L_β phase, as
488 shown by replicates #2 and #8 in smaller membranes (Fig. S3), and from the simulations of large
489 membranes (Figs. 5*b* and S9*a, b*). Therefore, there may be room for further optimization of the
490 MARTINI2On DPPC FF for accurate reproduction of low temperature phase behaviour.

491 Interestingly, when replicate #3 from Fig. S3 was equilibrated for 5 μs at 280 K, it showed
492 the formation of a weakly interdigitated titled domain (Fig. S11*a*), a potential precursor for the
493 formation of a true ripple phase. To assess this further, we set up a 6-times larger membrane
494 (Fig. S11*b*) by repeating the smaller system across periodic boundaries along the membrane
495 plane (similar to Fig. 5*a*). After 10 μs of constant temperature EQMD at 280 K, the interdigitation
496 almost completely disappeared as shown by the final MD snapshot (Fig. S11*b*) and corresponding
497 Voronoi-thickness maps (Fig. S11*c*).

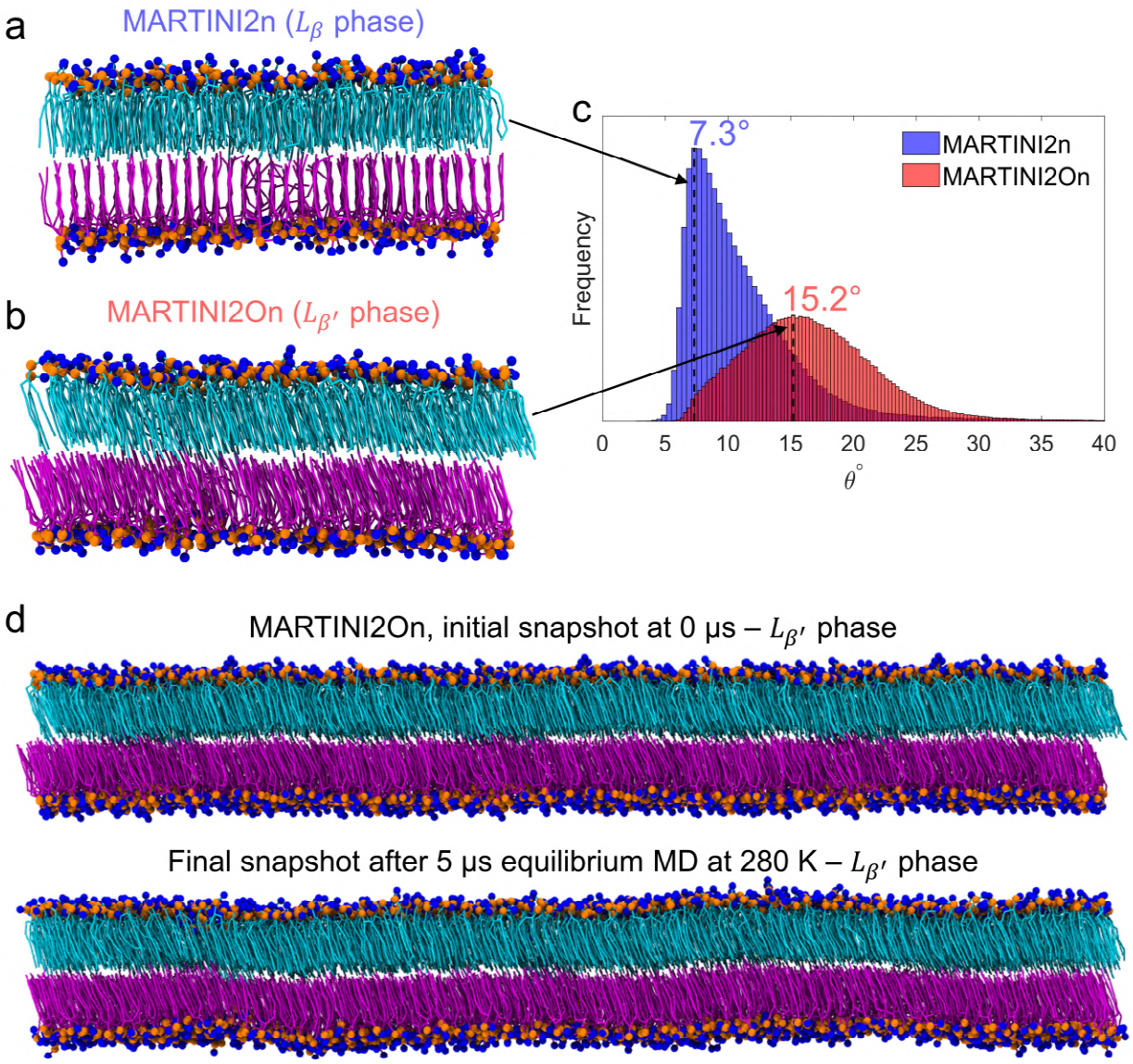

Fig. 6. Comparison of gel-phase structures of MARTINI membranes. Gel phase DPPC bilayer structures with **(a)** the standard MARTINI2n FF, and **(b)** the optimized MARTINI2On FF are shown. MARTINI2n membranes freeze into the straight gel phase (L_β) whereas MARTINI2On membranes often sample the tilted gel phase ($L_{\beta'}$), quantified by the lipid tilt-angle distributions **(c)**. **(d)** To confirm that this was a true thermodynamic phase and not a finite size effect, the smaller $L_{\beta'}$ membrane in (a) was replicated 6x (initial snapshot) and then equilibrated for 5 μs at 280 K. The membrane remained in the $L_{\beta'}$ phase thus ruling out finite size artefacts.

4 Summary and Conclusion

Molecular simulations at various levels of FF descriptions, ranging from all-atom and united atom models at the finer scales to DPD and MARTINI models at higher levels of coarse graining, have been extensively used to study the rich variety of equilibrium phases observed in model phospholipid bilayer membranes[1,17,76]. In particular, the rippled $P_{\beta'}$ phase, sensitive to initial configurations, annealing protocols, and finite-size effects, has been challenging to capture using MD simulations[20,25,34,41]. Although all-atom FFs have successfully captured the formation of the ripple phase (Table 1), the ability of the widely used MARTINI force-fields to stabilize this intermediate phase, which occurs below the main gel-to-liquid crystalline transition, has been a matter of some debate[34,47].

In this manuscript, we assessed the ability of MARTINI DPPC lipid membranes described by five MARTINI FF variants (see Introduction and Methods) towards capturing the ripple phase. Previous experiments[33,37–40] and all-atom simulations[19,30,43,44] have shown that DPPC membranes sample the tilted ripple phase at pre-transition temperatures. Previous MARTINI studies yielded conflicting observations, with some inferring that MARTINI DPPC lipid membranes could not capture the ripple state[34], while other studies observed otherwise[30,46,47]. Therefore, we established a standard simulated annealing-based MD protocol, built on insights from previous studies[18–20,30,43,44], for reliably producing the tilted ripple phase in multiple all-atom DPPC membrane MD replicates. By cooling from the fluid phase to below the phase transition followed by constant temperature equilibration. The structure of these rippled membranes resembled those from previous studies[19,20,43,44]. We then applied the same MD protocol to fluid phase MARTINI DPPC membranes with five MARTINI FF variants and ten independent MD replicates per variant. Simulations with all the five MARTINI FFs showed that a fraction of replicates formed interdigitated ripple-like states. These simulations also reinforced the importance of using multiple independent MD replicates for robustly observing phase behaviour[18,49]. The lateral orientation of

533 interdigitated domains in these ripple-like membranes were different compared to those from all-
534 atom simulations and resembled a membrane with co-existing interdigitated L_α and gel phases.

535 Next, we explored whether the MARTINI ripple-like membranes were kinetically trapped
536 states enforced by finite system size effects. To this end, we first re-established the all-atom
537 protocols by employing the aforementioned MD cooling protocol on large all-atom DPPC
538 membranes. We observed that these larger membranes also formed the tilted ripple phase with
539 reticulated interdigitated domains, in agreement with previously reported large-membrane all-
540 atom DPPC simulations[30,43]. However, when similarly large MARTINI DPPC membranes (3 FF
541 variants, 2 replicates each) were cooled from the fluid phase, they failed to capture ripple-like
542 states and froze directly into the gel phase . To confirm this behaviour via an orthogonal approach,
543 we created larger membranes from previously formed smaller ripple-like membranes, by
544 repeating them across periodic boundaries. These larger MARTINI periodic ripple-like
545 membranes (3 FF variants), with an initial configuration bias towards the ripple phase, were then
546 simulated at a constant temperature of 280 K, below the transition temperature. Strikingly, all the
547 membranes showed a progressive loss of the interdigitated ripple-like domains, and either
548 transitioned, or were in the process of transitioning, into the gel phase. Based on these findings
549 we attribute the ripple-like states observed in the smaller MARTINI membranes to finite size
550 artefacts. In the case of the MARTINI2On DPPC FF, the inability to form the tilted ripple was
551 despite its ability to capture the tilted gel phase at lower temperatures without the need for
552 enhanced sampling.

553 In summary, our observations systematically display that the current versions of MARTINI
554 DPPC FFs may not be able to capture the $P_{\beta'}$ phase, which involves an intricate interplay of lipid
555 tail interdigitation, tilt and headgroup hydration in the membrane. Specifically reparametrizing the
556 MARTINI FFs to better reproduce membrane thermodynamics and phase behaviour is expected
557 to yield CG models that may bridge the qualitative and quantitative gap towards all-atom MD

simulations, while unlocking the speed and scaling advantages associated with the versatile and powerful MARTINI framework.

Acknowledgements

We thank the Supercomputer Education and Research Center (SERC) computational facility at the Indian Institute of Science, Bengaluru, for access to supercomputing resources. K.G.A. acknowledges funding by a grant from the Department of Science and Technology, Government of India.

Author contributions

Conceptualization: R.D.; Data curation: P.S.; Formal analysis: R.D. and P.S.; Funding acquisition: K.G.A.; Investigation: P.S. and R.D.; Methodology: R.D. and P.S.; Project administration: P.S. and R.D.; Resources: P.S., R.D. and K.G.A.; Software (simulations, analysis code): P.S. and R.D.; Supervision: K.G.A.; Validation: P.S., R.D. and K.G.A.; Visualization: P.S. and R.D.; Writing – original draft: R.D. and P.S.; Writing – review & editing: R.D., P.S. and K.G.A.

All authors have given approval to the final version of the manuscript.

‡These authors (P.S. and R.D.) contributed equally.

Conflict of interest

The authors declare no conflicts of interest.

TOC/Abstract Graphic

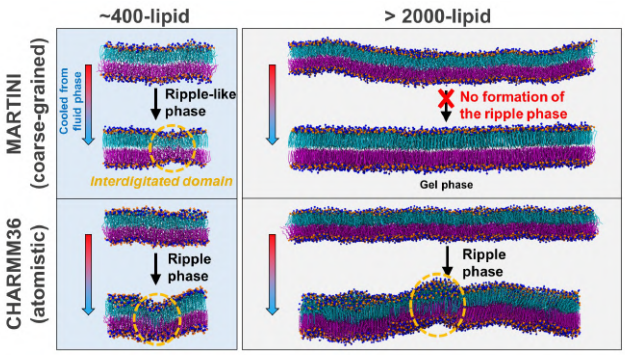

References

(1) Kulkarni, C. V. Lipid Crystallization: From Self-Assembly to Hierarchical and Biological Ordering. *Nanoscale* **2012**, *4* (19), 5779–5791.

(2) Nagle, J. F. Theory of the Main Lipid Bilayer Phase Transition. *Ann. Rev. Phys. Chem.* **1980**, *31* (1), 157–196.

(3) Harayama, T.; Riezman, H. Understanding the Diversity of Membrane Lipid Composition. *Nat. Rev. Mol. Cell Biol.* **2018**, *19* (5), 281–296.

(4) Kohli, A. G.; Kierstead, P. H.; Venditto, V. J.; Walsh, C. L.; Szoka, F. C. Designer Lipids for Drug Delivery: From Heads to Tails. *J. Control. Release* **2014**, *190*, 274–287.

(5) Anderson, M.; Omri, A. The Effect of Different Lipid Components on the in Vitro Stability and Release Kinetics of Liposome Formulations. *Drug. Deliv.* **2004**, *11* (1), 33–39.

(6) Kulkarni, A.; Chandrasekar, V.; Natarajan, S. K.; Ramesh, A.; Pandey, P.; Nirgud, J.; Bhatnagar, H.; Ashok, D.; Ajay, A. K.; Sengupta, S. A Designer Self-Assembled Supramolecule Amplifies Macrophage Immune Responses against Aggressive Cancer. *Nat. Biomed. Eng.* **2018**, *2* (8), 589–599.

(7) Phillips, R.; Ursell, T.; Wiggins, P.; Sens, P. Emerging Roles for Lipids in Shaping Membrane-Protein Function. *Nature* **2009**, *459* (7245), 379–385.

(8) Blicher, A.; Wodzinska, K.; Fidorra, M.; Winterhalter, M.; Heimburg, T. The Temperature Dependence of Lipid Membrane Permeability, Its Quantized Nature, and the Influence of Anesthetics. *Biophys. J.* **2009**, *96* (11), 4581–4591.

(9) Sharma, P.; Parthasarathi, S.; Patil, N.; Waskar, M.; Raut, J. S.; Puranik, M.; Ayappa, K. G.; Basu, J. K. Assessing Barriers for Antimicrobial Penetration in Complex Asymmetric Bacterial Membranes: A Case Study with Thymol. *Langmuir* **2020**, *36* (30), 8800–8814. https://doi.org/10.1021/acs.langmuir.0c01124.

(10) Perez-Isidoro, R.; Sierra-Valdez, F. J.; Ruiz-Suarez, J. C. Anesthetic Diffusion through Lipid Membranes Depends on the Protonation Rate. *Sci. Rep.* **2014**, *4*, 7534.

(11) Yilmaz, N.; Kobayashi, T. Assemblies of Pore-Forming Toxins Visualized by Atomic Force Microscopy. *Biochim. Biophys. Acta* **2016**, *1858* (3), 500–511.

(12) Rojko, N.; Anderluh, G. How Lipid Membranes Affect Pore Forming Toxin Activity. *Acc. Chem. Res.* **2015**, *48* (12), 3073–3079.

(13) Gerelli, Y.; Porcar, L.; Lombardi, L.; Fragneto, G. Lipid Exchange and Flip-Flop in Solid Supported Bilayers. *Langmuir* **2013**, *29* (41), 12762–12769.

(14) Pomorski, T. G.; Menon, A. K. Lipid Somersaults: Uncovering the Mechanisms of Protein-Mediated Lipid Flipping. *Prog. Lipid Res.* **2016**, *64*, 69–84.

(15) Andersen, S. S.; Jackson, A. D.; Heimburg, T. Towards a Thermodynamic Theory of Nerve Pulse Propagation. *Prog. Neurobiol.* **2009**, *88* (2), 104–113.

(16) de Smet, M.; Langereis, S.; van den Bosch, S.; Grull, H. Temperature-Sensitive Liposomes for Doxorubicin Delivery under MRI Guidance. *J. Control. Release* **2010**, *143* (1), 120–127.

(17) Enkavi, G.; Javanainen, M.; Kulig, W.; Róg, T.; Vattulainen, I. Multiscale Simulations of Biological Membranes: The Challenge To Understand Biological Phenomena in a Living Substance. *Chem. Rev.* **2019**, *119* (9), 5607–5774. https://doi.org/10.1021/acs.chemrev.8b00538.

(18) Sun, L.; Böckmann, R. A. Membrane Phase Transition during Heating and Cooling: Molecular Insight into Reversible Melting. *European Biophysics Journal* **2018**, *47* (2), 151–164.

(19) Vries, A. H. de; Yefimov, S.; Mark, A. E.; Marrink, S. J. Molecular Structure of the Lecithin Ripple Phase. *PNAS* **2005**, *102* (15), 5392–5396. https://doi.org/10.1073/pnas.0408249102.

(20) Lenz, O.; Schmid, F. Structure of Symmetric and Asymmetric ``Ripple'' Phases in Lipid Bilayers. *Phys. Rev. Lett.* **2007**, *98* (5), 058104. https://doi.org/10.1103/PhysRevLett.98.058104.

(21) Kranenburg, M.; Smit, B. Phase Behavior of Model Lipid Bilayers. *J. Phys. Chem. B* **2005**, *109* (14), 6553–6563. https://doi.org/10.1021/jp0457646.

(22) Marrink, S. J.; Tieleman, D. P. Perspective on the Martini Model. *Chem. Soc. Rev.* **2013**, *42* (16), 6801–6822.

(23) Marrink, S. J.; Risselada, H. J.; Yefimov, S.; Tieleman, D. P.; de Vries, A. H. The MARTINI Force Field: Coarse Grained Model for Biomolecular Simulations. *The Journal of Physical Chemistry B* **2007**, *111* (27), 7812–7824.

641 (24) Bruininks, B. M. H.; Souza, P. C. T.; Marrink, S. J. A Practical View of the Martini Force
642 Field. In *Biomolecular Simulations: Methods and Protocols*; Bonomi, M., Camilloni, C.,
643 Eds.; Methods in Molecular Biology; Springer: New York, NY, 2019; pp 105–127.
644 https://doi.org/10.1007/978-1-4939-9608-7_5.

645 (25) Srivastava, A.; Debnath, A. Asymmetry and Rippling in Mixed Surfactant Bilayers from All-
646 Atom and Coarse-Grained Simulations: Interdigitation and Per Chain Entropy†. *The*
647 *Journal of Physical Chemistry B* **2020**. https://doi.org/10.1021/acs.jpcb.0c03761.

648 (26) Vaiwala, R.; Sharma, P.; Puranik, M.; Ayappa, K. G. Developing a Coarse-Grained Model
649 for Bacterial Cell Walls: Evaluating Mechanical Properties and Free Energy Barriers. *J.*
650 *Chem. Theory Comput.* **2020**, *16* (8), 5369–5384.
651 https://doi.org/10.1021/acs.jctc.0c00539.

652 (27) Ingólfsson, H. I.; Melo, M. N.; van Eerden, F. J.; Arnarez, C.; Lopez, C. A.; Wassenaar, T.
653 A.; Periole, X.; de Vries, A. H.; Tieleman, D. P.; Marrink, S. J. Lipid Organization of the
654 Plasma Membrane. *J. Am. Chem. Soc.* **2014**, *136* (41), 14554–14559.
655 https://doi.org/10.1021/ja507832e.

656 (28) Alessandri, R.; Souza, P. C. T.; Thallmair, S.; Melo, M. N.; de Vries, A. H.; Marrink, S. J.
657 Pitfalls of the Martini Model. *J. Chem. Theory Comput.* **2019**, *15* (10), 5448–5460.
658 https://doi.org/10.1021/acs.jctc.9b00473.

659 (29) Desikan, R.; Patra, S. M.; Sarthak, K.; Maiti, P. K.; Ayappa, K. G. Comparison of Coarse-
660 Grained (MARTINI) and Atomistic Molecular Dynamics Simulations of α and β Toxin
661 Nanopores in Lipid Membranes. *J. Chem. Sci.* **2017**, *129* (7), 1017–1030.
662 https://doi.org/10.1007/s12039-017-1316-0.

663 (30) Carpenter, T. S.; López, C. A.; Neale, C.; Montour, C.; Ingólfsson, H. I.; Di Natale, F.;
664 Lightstone, F. C.; Gnanakaran, S. Capturing Phase Behavior of Ternary Lipid Mixtures
665 with a Refined Martini Coarse-Grained Force Field. *J. Chem. Theory Comput.* **2018**, *14*
666 (11), 6050–6062. https://doi.org/10.1021/acs.jctc.8b00496.

667 (31) Globisch, C.; Krishnamani, V.; Deserno, M.; Peter, C. Optimization of an Elastic Network
668 Augmented Coarse Grained Model to Study CCMV Capsid Deformation. *PLoS ONE*
669 **2013**, *8* (4), e60582.

670 (32) Biltonen, R. L.; Lichtenberg, D. The Use of Differential Scanning Calorimetry as a Tool to
671 Characterize Liposome Preparations. *Chem. Phys. Lipids* **1993**, *64* (1), 129–142.

672 (33) Tardieu, A.; Luzzati, V.; Reman, F. C. Structure and Polymorphism of the Hydrocarbon
673 Chains of Lipids: A Study of Lecithin-Water Phases. *Journal of Molecular Biology* **1973**, *75*
674 (4), 711–733. https://doi.org/10.1016/0022-2836(73)90303-3.

675 (34) Rodgers, J. M.; Sorensen, J.; de Meyer, F. J.; Schiott, B.; Smit, B. Understanding the
676 Phase Behavior of Coarse-Grained Model Lipid Bilayers through Computational
677 Calorimetry. *J. Phys. Chem. B* **2012**, *116* (5), 1551–1569.

678 (35) Riske, K. A.; Barroso, R. P.; Vequi-Suplicy, C. C.; Germano, R.; Henriques, V. B.; Lamy,
679 M. T. Lipid Bilayer Pre-Transition as the Beginning of the Melting Process. *Biochimica et*

Biophysica Acta (BBA) - Biomembranes **2009**, *1788* (5), 954–963. https://doi.org/10.1016/j.bbamem.2009.01.007.

(36) Heimburg, T. A Model for the Lipid Pretransition: Coupling of Ripple Formation with the Chain-Melting Transition. *Biophys. J.* **2000**, *78* (3), 1154–1165. https://doi.org/10.1016/S0006-3495(00)76673-2.

(37) Sun, W. J.; Tristram-Nagle, S.; Suter, R. M.; Nagle, J. F. Structure of the Ripple Phase in Lecithin Bilayers. *PNAS* **1996**, *93* (14), 7008–7012. https://doi.org/10.1073/pnas.93.14.7008.

(38) Katsaras, J.; Tristram-Nagle, S.; Liu, Y.; Headrick, R. L.; Fontes, E.; Mason, P. C.; Nagle, J. F. Clarification of the Ripple Phase of Lecithin Bilayers Using Fully Hydrated, Aligned Samples. *Phys. Rev. E* **2000**, *61* (5), 5668–5677. https://doi.org/10.1103/PhysRevE.61.5668.

(39) Sengupta, K.; Raghunathan, V. A.; Katsaras, J. Structure of the Ripple Phase of Phospholipid Multibilayers. *Phys. Rev. E* **2003**, *68* (3), 031710. https://doi.org/10.1103/PhysRevE.68.031710.

(40) Kamal, M. A.; Raghunathan, V. Naphthalene Derivatives Induce Acyl Chain Interdigitation in Dipalmitoylphosphatidylcholine Bilayers. *The Journal of Physical Chemistry B* **2016**, *120* (1), 164–172.

(41) Debnath, A.; Thakkar, F. M.; Maiti, P. K.; Kumaran, V.; Ayappa, K. G. Laterally Structured Ripple and Square Phases with One and Two Dimensional Thickness Modulations in a Model Bilayer System. *Soft Matter* **2014**, *10* (38), 7630–7637. https://doi.org/10.1039/C4SM01031K.

(42) Pluhackova, K.; Kirsch, S. A.; Han, J.; Sun, L.; Jiang, Z.; Unruh, T.; Böckmann, R. A. A Critical Comparison of Biomembrane Force Fields: Structure and Dynamics of Model DMPC, POPC, and POPE Bilayers. *J. Phys. Chem. B* **2016**, *120* (16), 3888–3903. https://doi.org/10.1021/acs.jpcb.6b01870.

(43) Kirsch, S. A.; Böckmann, R. A. Coupling of Membrane Nanodomain Formation and Enhanced Electroporation near Phase Transition. *Biophysical Journal* **2019**, *116* (11), 2131–2148. https://doi.org/10.1016/j.bpj.2019.04.024.

(44) Khakbaz, P.; Klauda, J. B. Investigation of Phase Transitions of Saturated Phosphocholine Lipid Bilayers via Molecular Dynamics Simulations. *Biochimica et Biophysica Acta (BBA) - Biomembranes* **2018**, *1860* (8), 1489–1501. https://doi.org/10.1016/j.bbamem.2018.04.014.

(45) Debnath, A.; Ayappa, K. G.; Kumaran, V.; Maiti, P. K. The Influence of Bilayer Composition on the Gel to Liquid Crystalline Transition. *J. Phys. Chem. B* **2009**, *113* (31), 10660–10668. https://doi.org/10.1021/jp901551d.

(46) Lin, X.; Gu, N. Surface Properties of Encapsulating Hydrophobic Nanoparticles Regulate the Main Phase Transition Temperature of Lipid Bilayers: A Simulation Study. *Nano Res.* **2014**, *7* (8), 1195–1204. https://doi.org/10.1007/s12274-014-0482-3.

(47) Stelter, D.; Keyes, T. Enhanced Sampling of Phase Transitions in Coarse-Grained Lipid Bilayers. *J. Phys. Chem. B* **2017**, *121* (23), 5770–5780. https://doi.org/10.1021/acs.jpcb.6b11711.

(48) Yesylevskyy, S. O.; Schäfer, L. V.; Sengupta, D.; Marrink, S. J. Polarizable Water Model for the Coarse-Grained MARTINI Force Field. *PLoS Comput Biol* **2010**, *6* (6), 1–17.

(49) Grossfield, A.; Patrone, P. N.; Roe, D. R.; Schultz, A. J.; Siderius, D.; Zuckerman, D. M. Best Practices for Quantification of Uncertainty and Sampling Quality in Molecular Simulations [Article v1.0]. *Living Journal of Computational Molecular Science* **2018**, *1* (1), 5067. https://doi.org/10.33011/livecoms.1.1.5067.

(50) Jo, S.; Kim, T.; Iyer, V. G.; Im, W. CHARMM-GUI: A Web-Based Graphical User Interface for CHARMM. *J Comput Chem* **2008**, *29* (11), 1859–1865. https://doi.org/10.1002/jcc.20945.

(51) Lee, J.; Cheng, X.; Swails, J. M.; Yeom, M. S.; Eastman, P. K.; Lemkul, J. A.; Wei, S.; Buckner, J.; Jeong, J. C.; Qi, Y.; Jo, S.; Pande, V. S.; Case, D. A.; Brooks, C. L.; MacKerell, A. D.; Klauda, J. B.; Im, W. CHARMM-GUI Input Generator for NAMD, GROMACS, AMBER, OpenMM, and CHARMM/OpenMM Simulations Using the CHARMM36 Additive Force Field. *J. Chem. Theory Comput.* **2016**, *12* (1), 405–413. https://doi.org/10.1021/acs.jctc.5b00935.

(52) Wu, E. L.; Cheng, X.; Jo, S.; Rui, H.; Song, K. C.; Dávila-Contreras, E. M.; Qi, Y.; Lee, J.; Monje-Galvan, V.; Venable, R. M.; Klauda, J. B.; Im, W. CHARMM-GUI Membrane Builder toward Realistic Biological Membrane Simulations. *J Comput Chem* **2014**, *35* (27), 1997–2004. https://doi.org/10.1002/jcc.23702.

(53) Meyer, H. W. Pretransition-Ripples in Bilayers of Dipalmitoylphosphatidylcholine: Undulation or Periodic Segments? A Freeze-Fracture Study. *Biochimica et Biophysica Acta (BBA) - Lipids and Lipid Metabolism* **1996**, *1302* (2), 138–144. https://doi.org/10.1016/0005-2760(96)00054-9.

(54) Pastor, R. W.; MacKerell, A. D. Development of the CHARMM Force Field for Lipids. *J. Phys. Chem. Lett.* **2011**, *2* (13), 1526–1532. https://doi.org/10.1021/jz200167q.

(55) Klauda, J. B.; Venable, R. M.; Freites, J. A.; O'Connor, J. W.; Tobias, D. J.; Mondragon-Ramirez, C.; Vorobyov, I.; MacKerell, A. D.; Pastor, R. W. Update of the CHARMM All-Atom Additive Force Field for Lipids: Validation on Six Lipid Types. *J. Phys. Chem. B* **2010**, *114* (23), 7830–7843.

(56) Abraham, M. J.; Murtola, T.; Schulz, R.; Páll, S.; Smith, J. C.; Hess, B.; Lindahl, E. GROMACS: High Performance Molecular Simulations through Multi-Level Parallelism from Laptops to Supercomputers. *SoftwareX* **2015**, *1*, 19–25.

(57) Braun, E.; Gilmer, J.; Mayes, H. B.; Mobley, D. L.; Monroe, J. I.; Prasad, S.; Zuckerman, D. M. Best Practices for Foundations in Molecular Simulations [Article v1.0]. *Living Journal of Computational Molecular Science* **2018**, *1* (1), 5957. https://doi.org/10.33011/livecoms.1.1.5957.

(58) Smith, D. J.; Klauda, J. B.; Sodt, A. J. Simulation Best Practices for Lipid Membranes [Article v1.0]. *Living Journal of Computational Molecular Science* **2018**, *1* (1), 5966. https://doi.org/10.33011/livecoms.1.1.5966.

(59) Lemkul, J. From Proteins to Perturbed Hamiltonians: A Suite of Tutorials for the GROMACS-2018 Molecular Simulation Package [Article v1.0]. *Living Journal of Computational Molecular Science* **2018**, *1* (1), 5068. https://doi.org/10.33011/livecoms.1.1.5068.

(60) Desikan, R.; Behera, A.; Maiti, P. K.; Ayappa, K. G. Using Multiscale Molecular Dynamics Simulations to Obtain Insights into Pore Forming Toxin Mechanisms. *arXiv:2010.13854 [cond-mat]* **2020**.

(61) Darden, T.; York, D.; Pedersen, L. Particle Mesh Ewald: An N.Log(N) Method for Ewald Sums in Large Systems. *J. Chem. Phys.* **1993**, *98* (12), 10089–10092.

(62) Hess, B. P-LINCS: A Parallel Linear Constraint Solver for Molecular Simulation. *J. Chem. Theory. Comput.* **2008**, *4* (1), 116–122.

(63) Bussi, G.; Donadio, D.; Parrinello, M. Canonical Sampling through Velocity Rescaling. *The Journal of chemical physics* **2007**, *126* (1), 014101.

(64) Parrinello, M.; Rahman, A. Polymorphic Transitions in Single Crystals: A New Molecular Dynamics Method. *Journal of Applied Physics* **1981**, *52* (12), 7182–7190.

(65) Alavi, S.; Thompson, D. L. Molecular Dynamics Studies of Melting and Some Liquid-State Properties of 1-Ethyl-3-Methylimidazolium Hexafluorophosphate [Emim][PF6]. *J. Chem. Phys.* **2005**, *122* (15), 154704.

(66) Zhang, Y.; Maginn, E. J. A Comparison of Methods for Melting Point Calculation Using Molecular Dynamics Simulations. *J. Chem. Phys.* **2012**, *136* (14), 144116. https://doi.org/10.1063/1.3702587.

(67) Wassenaar, T. A.; Ingólfsson, H. I.; Böckmann, R. A.; Tieleman, D. P.; Marrink, S. J. Computational Lipidomics with Insane: A Versatile Tool for Generating Custom Membranes for Molecular Simulations. *Journal of chemical theory and computation* **2015**, *11* (5), 2144–2155.

(68) de Jong, D. H.; Baoukina, S.; Ingólfsson, H. I.; Marrink, S. J. Martini Straight: Boosting Performance Using a Shorter Cutoff and GPUs. *Comput. Phys. Commun.* **2016**, *199*, 1–7. https://doi.org/10.1016/j.cpc.2015.09.014.

(69) Tironi, I. G.; Sperb, R.; Smith, P. E.; van Gunsteren, W. F. A Generalized Reaction Field Method for Molecular Dynamics Simulations. *The Journal of chemical physics* **1995**, *102* (13), 5451–5459.

(70) Humphrey, W.; Dalke, A.; Schulten, K. VMD: Visual Molecular Dynamics. *Journal of Molecular Graphics* **1996**, *14* (1), 33–38.

(71) Guixà-González, R.; Rodriguez-Espigares, I.; Ramírez-Anguita, J. M.; Carrió-Gaspar, P.; Martinez-Seara, H.; Giorgino, T.; Selent, J. MEMBPLUGIN: Studying Membrane Complexity in VMD. *Bioinformatics* **2014**, *30* (10), 1478–1480. https://doi.org/10.1093/bioinformatics/btu037.

(72) Varadarajan, V.; Desikan, R.; Ayappa, K. G. Assessing the Extent of the Structural and Dynamic Modulation of Membrane Lipids Due to Pore Forming Toxins: Insights from Molecular Dynamics Simulations. *Soft Matter* **2020**, *16* (20), 4840–4857. https://doi.org/10.1039/D0SM00086H.

(73) Souza, P. C. T.; Thallmair, S.; Conflitti, P.; Ramírez-Palacios, C.; Alessandri, R.; Raniolo, S.; Limongelli, V.; Marrink, S. J. Protein–Ligand Binding with the Coarse-Grained Martini Model. *Nature Communications* **2020**, *11* (1), 3714. https://doi.org/10.1038/s41467-020-17437-5.

(74) Koynova, R.; Caffrey, M. Phases and Phase Transitions of the Hydrated Phosphatidylethanolamines. *Chemistry and Physics of Lipids* **1994**, *69* (1), 1–34. https://doi.org/10.1016/0009-3084(94)90024-8.

(75) Nagai, T.; Okamoto, Y. Replica-Exchange Molecular Dynamics Simulation of a Lipid Bilayer System with a Coarse-Grained Model. *Molecular Simulation* **2012**, *38* (5), 437–441. https://doi.org/10.1080/08927022.2011.564172.

(76) Manna, M.; Nieminen, T.; Vattulainen, I. Understanding the Role of Lipids in Signaling Through Atomistic and Multiscale Simulations of Cell Membranes. *Annu. Rev. Biophys.* **2019**, *48* (1), 421–439. https://doi.org/10.1146/annurev-biophys-052118-115553.

Supplementary information

Evaluating coarse-grained MARTINI force-fields for capturing the ripple phase of lipid membranes

***Pradyumn Sharma*[1,‡]*, Rajat Desikan*[1,‡,†]*, K. Ganapathy Ayappa*[1,2,*]**

[1]Department of Chemical Engineering, Indian Institute of Science, Bengaluru, India

[2]Centre for BioSystems Science and Engineering, Indian Institute of Science, Bengaluru, India

[‡]Co-first authors

[†]Present address: Certara QSP, Certara UK Limited, Sheffield, UK

*Corresponding author: K. Ganapathy Ayappa; E-mail: ayappa@iisc.ac.in

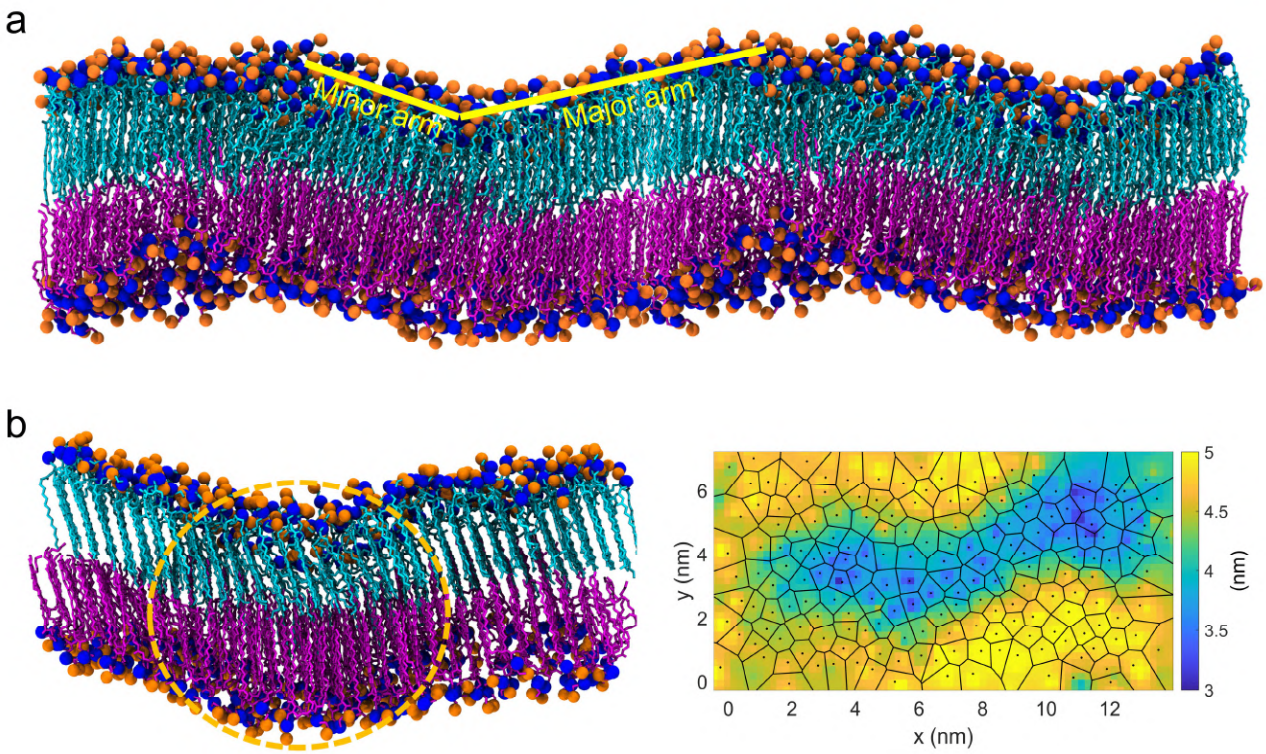

Fig. S1. An independent all-atom MD replicate reproduces the ripple phase. (a) MD snapshot at time point IV from Fig. 1*a* is periodically repeated along the x-axis, and the major and minor arms of the ripple in the upper leaflet are visually annotated for clarity. **(b)** Final snapshot (time point IV in Fig. 1) and corresponding Voronoi-thickness diagram from the independent simulated cooling replicate, using the same MD protocol as for the replicate in Fig. 1, shows robust reproduction of the tilted ripple phase from all-atom simulations.

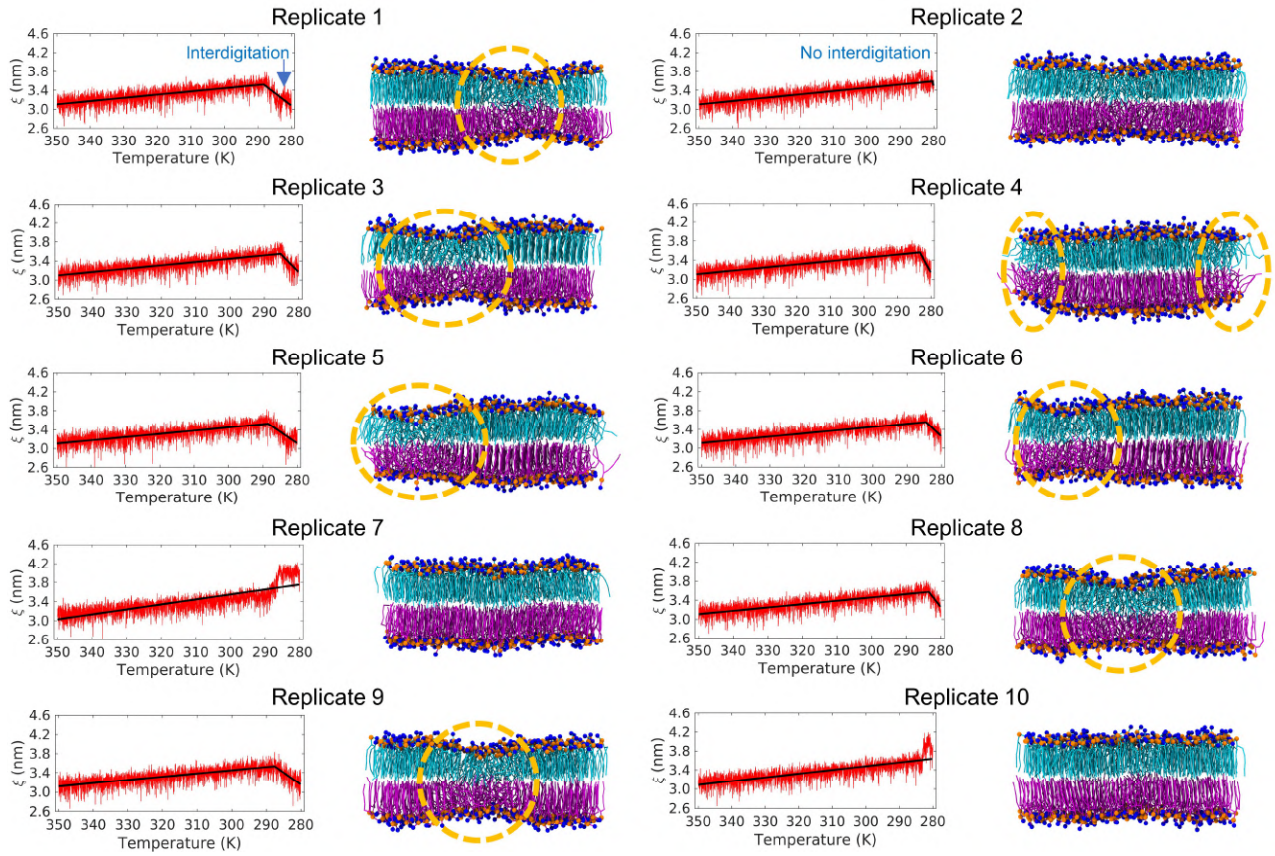

Fig. S2. Summary of 10 independent cooling MD replicates with the MARTINI2n FF. Temporal evolution of the minimum inter-leaflet P-P distance (ξ), a measure of the extent of interdigitation (Fig. 1*b*; $m_2 < 0$ – interdigitation, and $m_2 > 0$ – no interdigitation (Methods, Eq. 1), are highlighted in replicates 1 and 2, respectively). Final snapshots corresponding to time point III at the end of cooling simulations with MARTINI2n DPPC membranes are shown for all the 10 independent MD replicates. The interdigitated domains in replicates which exhibit ripple-like structures are marked with yellow dashed circles.

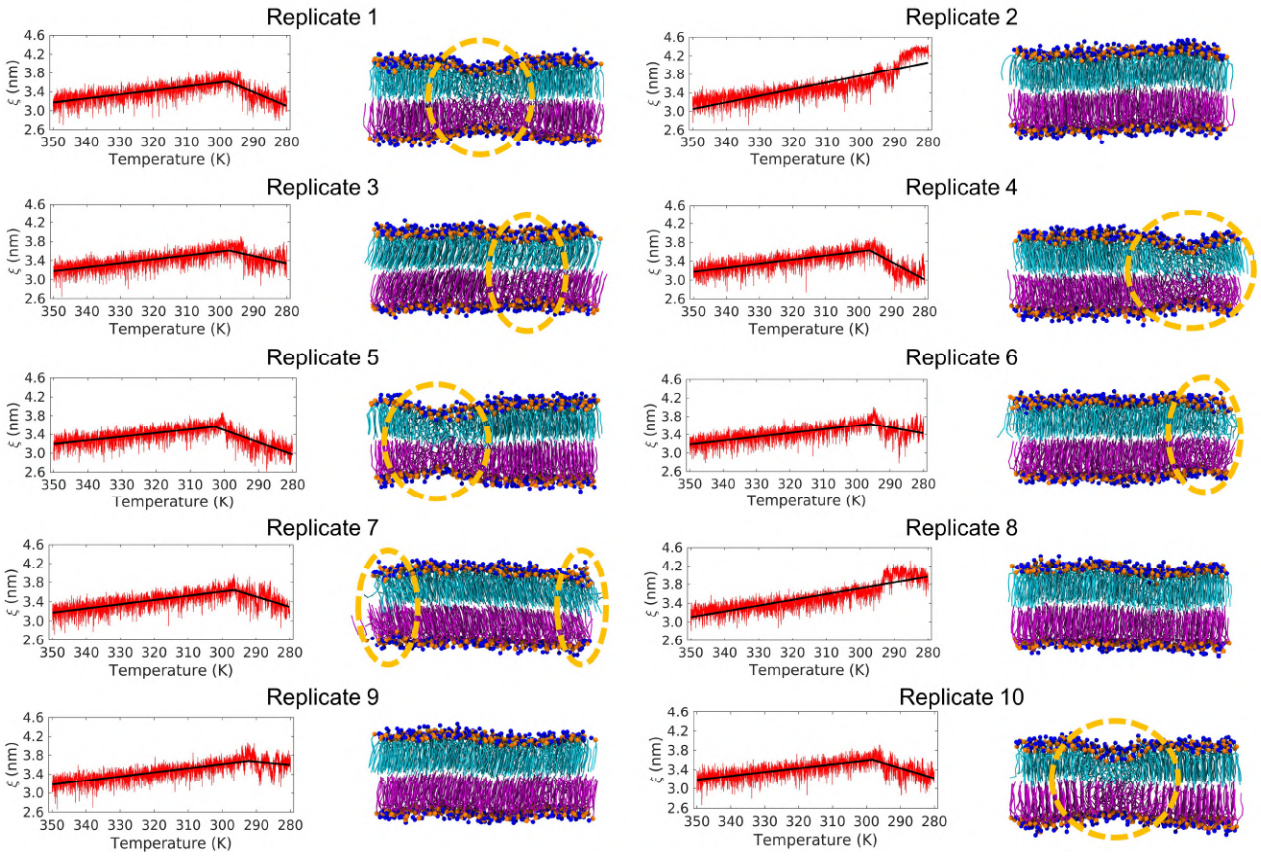

Fig. S3. Summary of 10 independent cooling MD replicates with the MARTINI2On FF. Same as Fig. S2, but with the MARTINI2On FF variant.

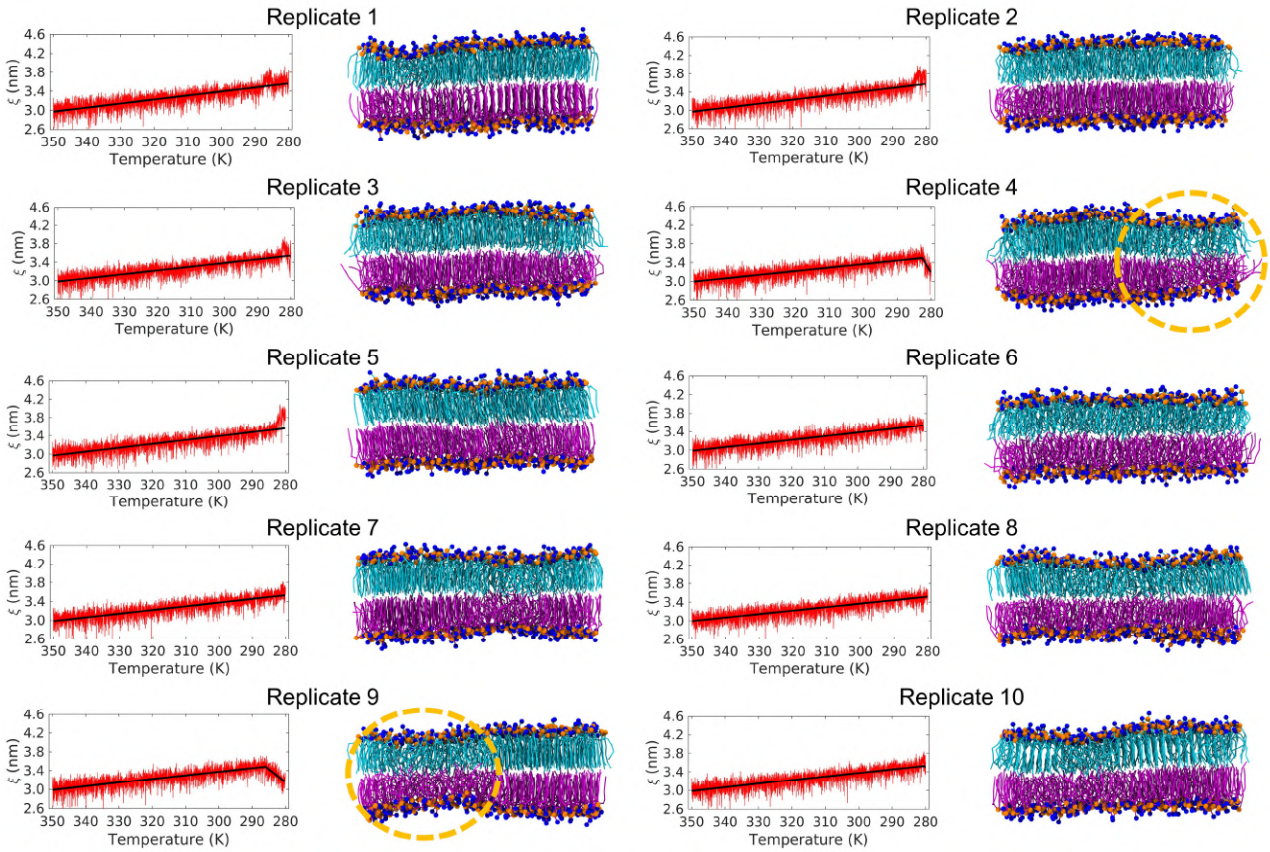

Fig. S4. Summary of 10 independent cooling MD replicates with the MARTINI3b FF. Same as Fig. S2, but with the MARTINI3b FF variant.

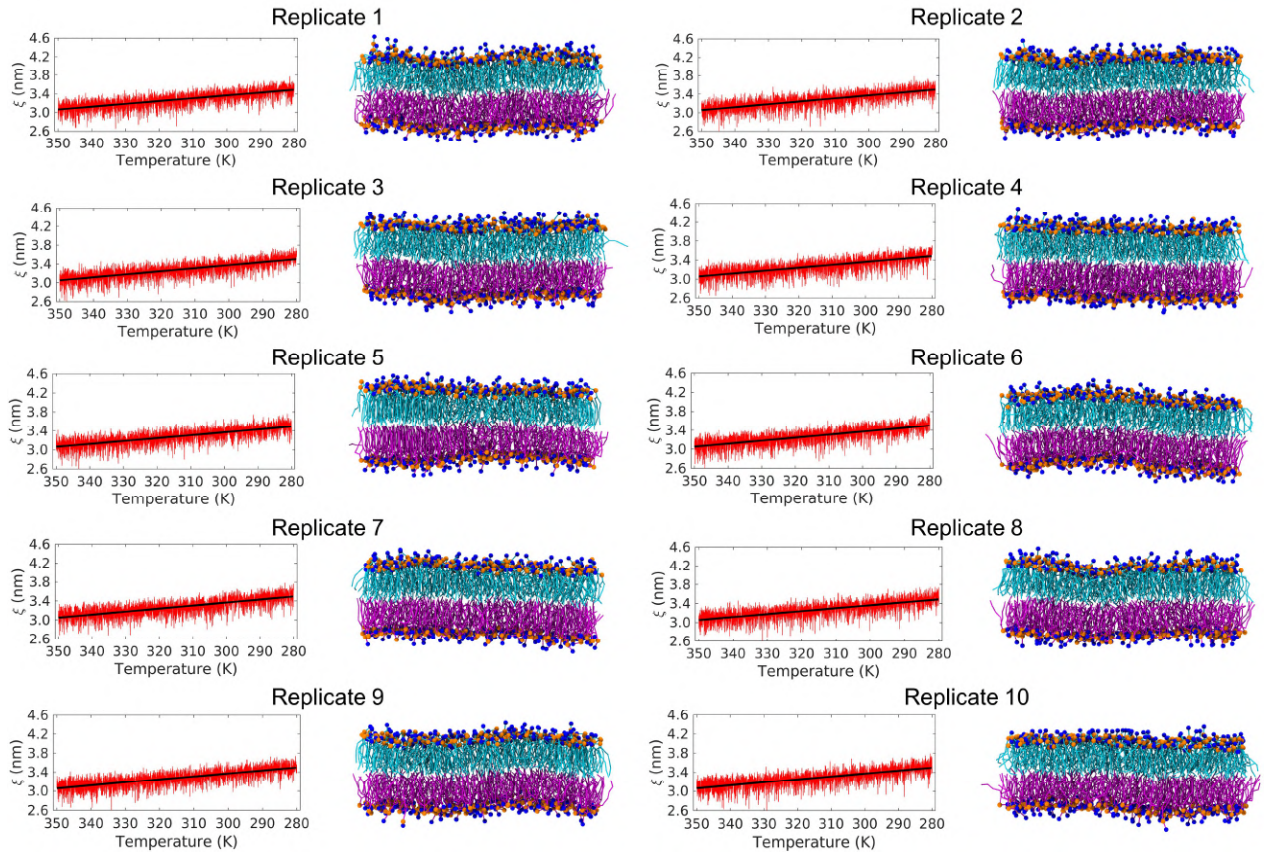

Fig. S5. Summary of 10 independent cooling MD replicates with the MARTINI2p FF. Same as Fig. S2, but with the MARTINI2p FF variant. Note that while none of the *ξ* plots show ripple-like domain formation during the cooling phase, replicate 5 formed shallow interdigitated ripple-like domains during the 5 μs EQMD (Fig. 2*f*).

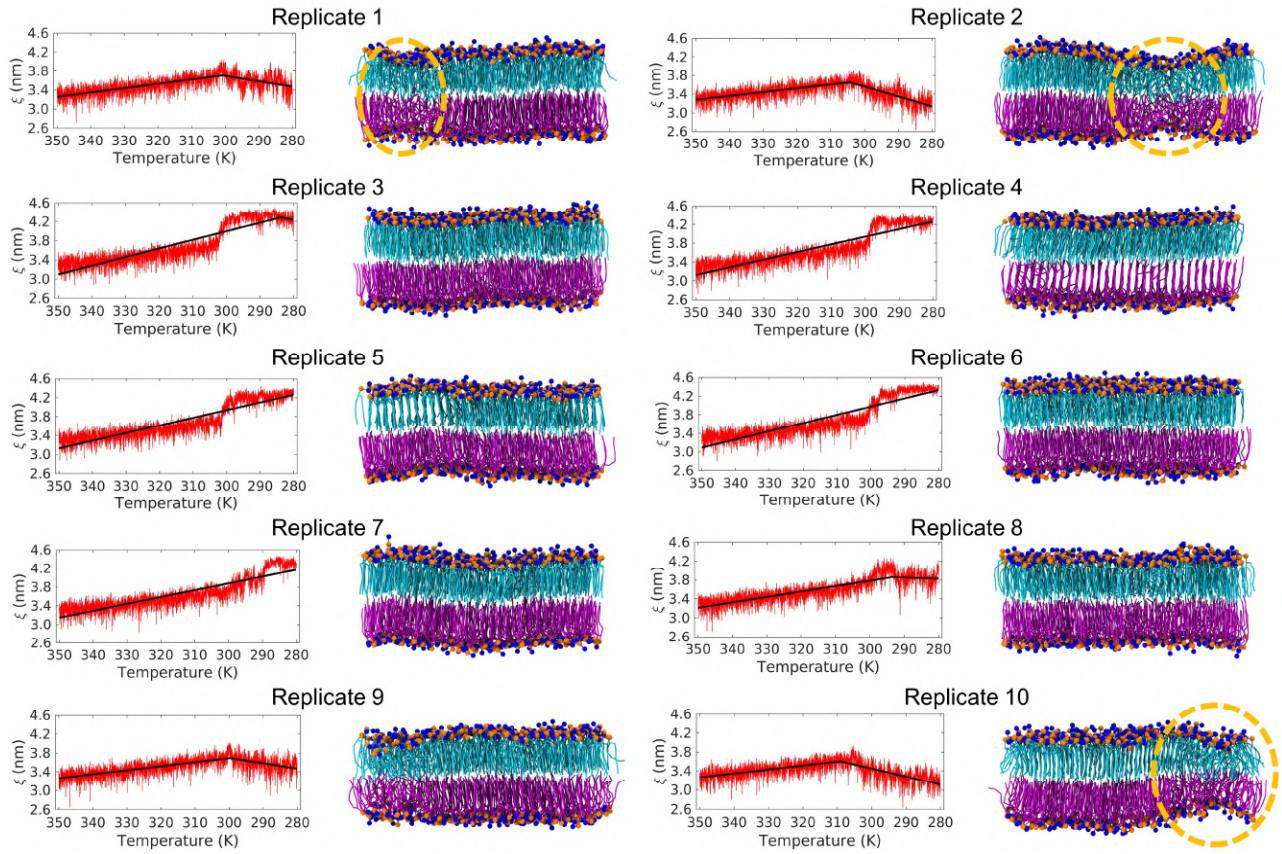

Fig. S6. Summary of 10 independent cooling MD replicates with the MARTINI2Op FF. Same as Fig. S2, but with the MARTINI2Op FF variant.

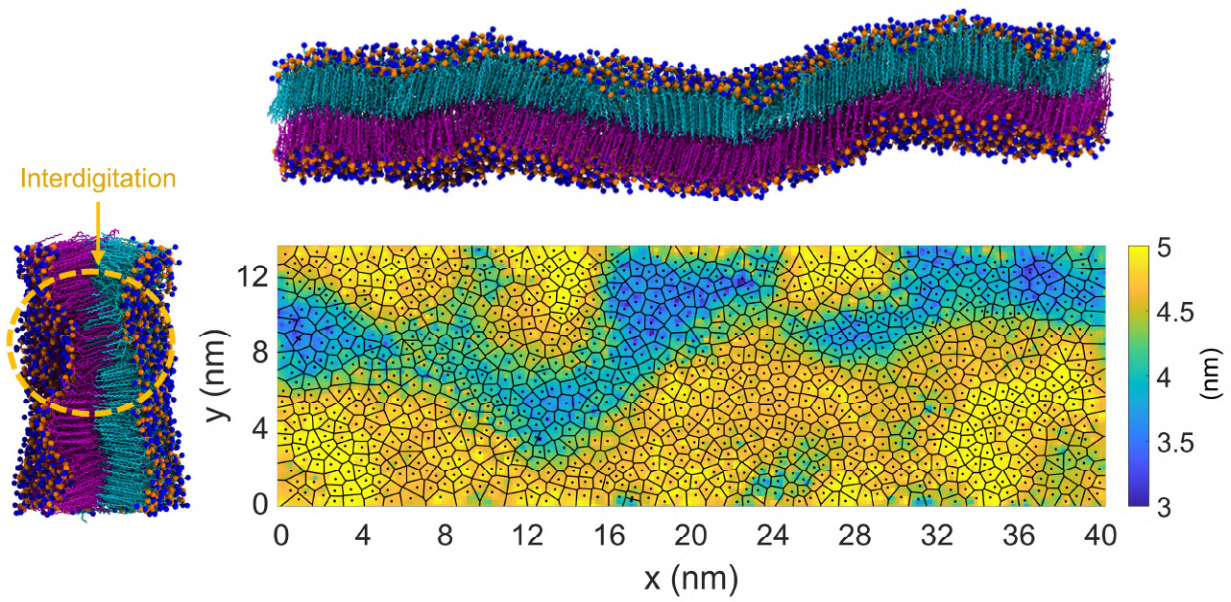

Fig. S7. Independent all-atom simulation replicate also shows ripple formation in a large DPPC membrane. Similar to Fig. 3, the final snapshot (front view) of a large DPPC membrane after being cooled to 290 K, and its corresponding Voronoi-thickness map, show the formation of symmetric, and asymmetric-interdigitated, ripple structures along the X-axis (shorter box dimension) and Y-axis (shorter box dimension), respectively. Note that the non-interdigitated symmetric ripple along the X-axis is indiscernible from the Voronoi-thickness map.

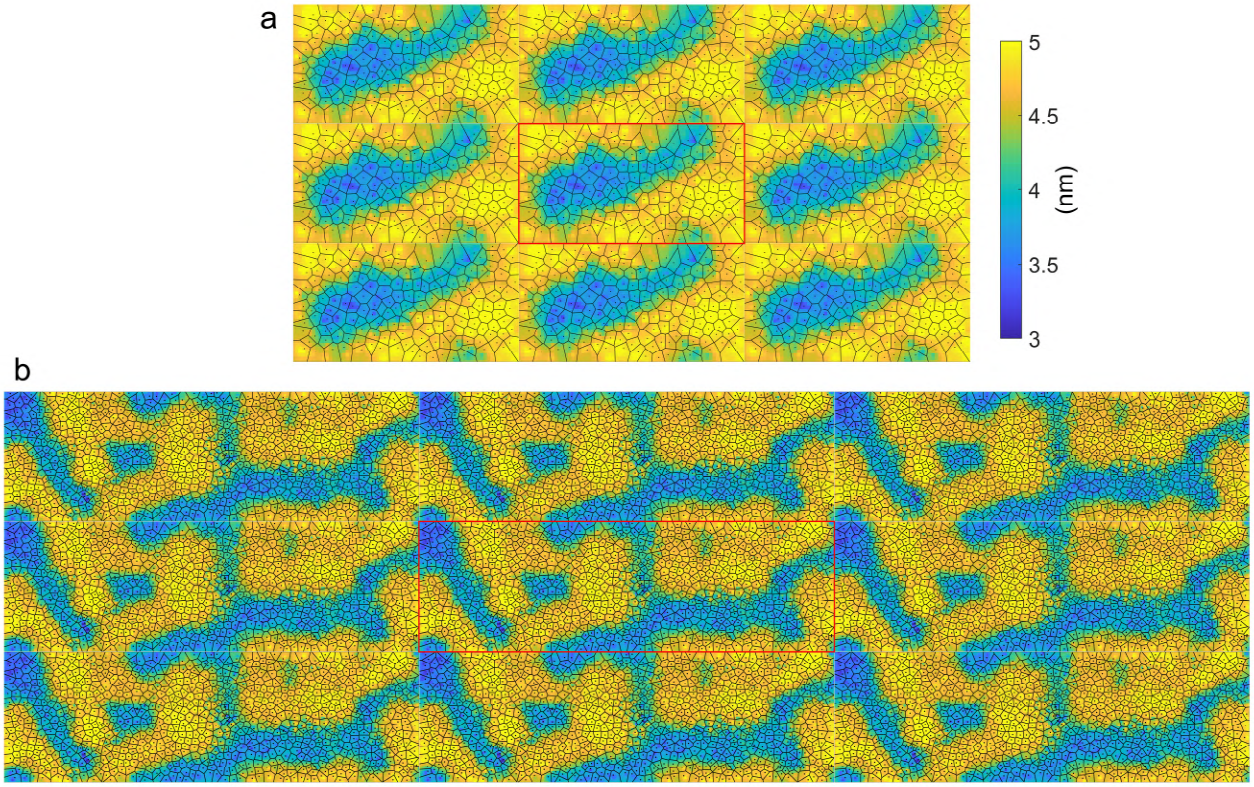

Fig. S8. Periodically repeated Voronoi-thickness modulation heatmaps of atomistic DPPC membranes. Voronoi-thickness modulation heatmaps after simulated cooling of atomistic **(a)** 368-lipid (Fig. 1), and **(b)** 2208-lipid (Fig. 3) DPPC membranes are shown with periodic images (original simulation box in the middle shown with a red border; same thickness colorbar applies for both systems). The reticulated interdigitated domains in the larger membrane contrast with the island-like isolated domains in the smaller membrane.

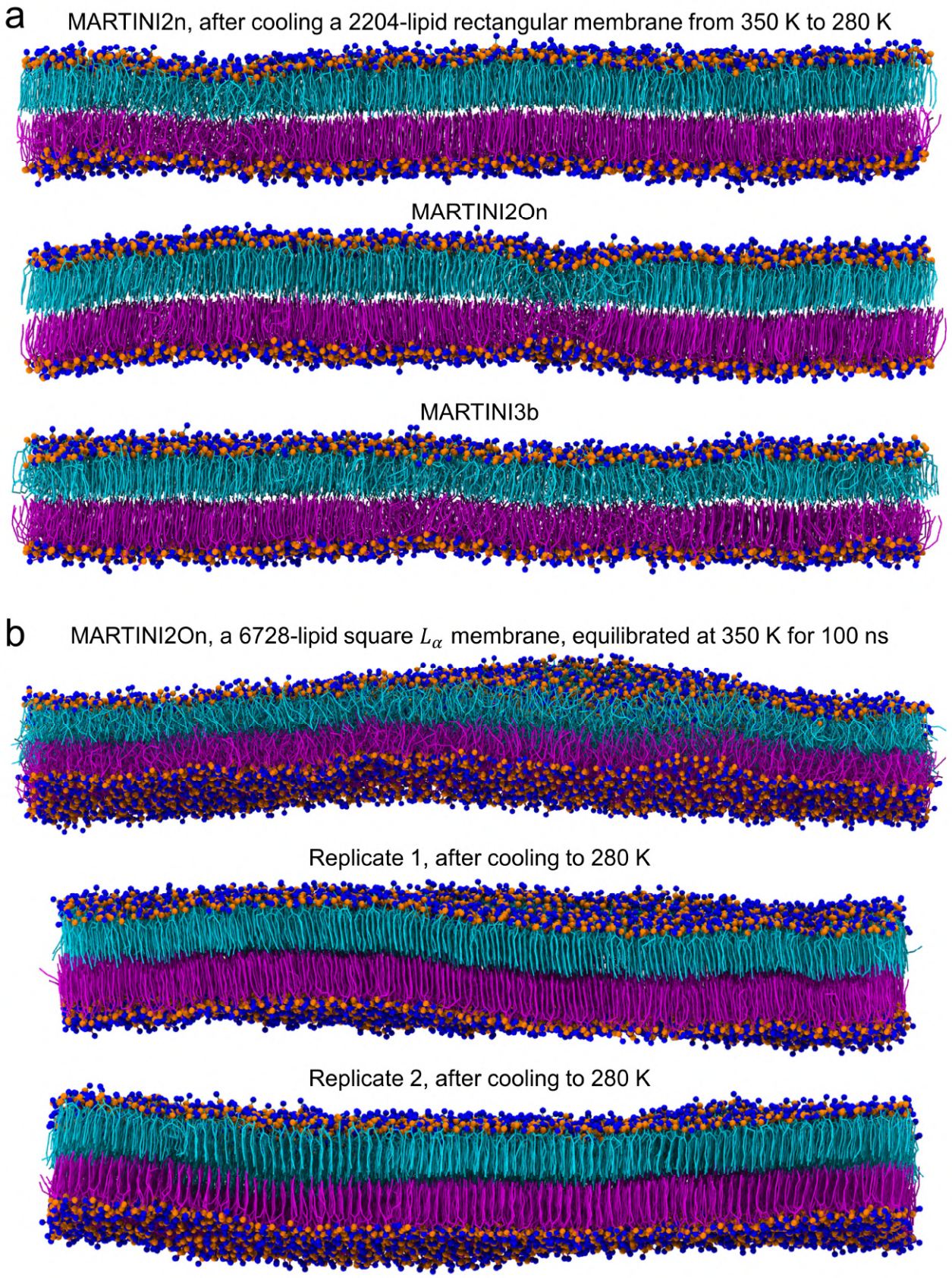
a
MARTINI2n, after cooling a 2204-lipid rectangular membrane from 350 K to 280 K
MARTINI2On
MARTINI3b
b
MARTINI2On, a 6728-lipid square L_α membrane, equilibrated at 350 K for 100 ns
Replicate 1, after cooling to 280 K
Replicate 2, after cooling to 280 K

Fig. S9 Independent MD replicates also exhibit lack of ripple formation in large MARTINI DPPC membranes. (a) Independent MD replicates similar to Fig. 4, where large, rectangular, MARTINI2n, MARTINI2On and MARTINI3b DPPC membranes, initially pre-equilibrated in the fluid phase at 350 K, exhibited direct transformation into the straight gel phase upon cooling to 280 K without forming either interdigitated or symmetric ripple-like structures (unlike the behaviour for smaller MARTINI membranes in Fig. 2). **(b)** The influence of membrane geometry was also tested by cooling two large, square, MARTINI2On membrane replicates, from 350 K to 280 K. Similar to the rectangular membrane patches, both square membrane replicates directly froze into the gel phase without forming ripple-like structures.

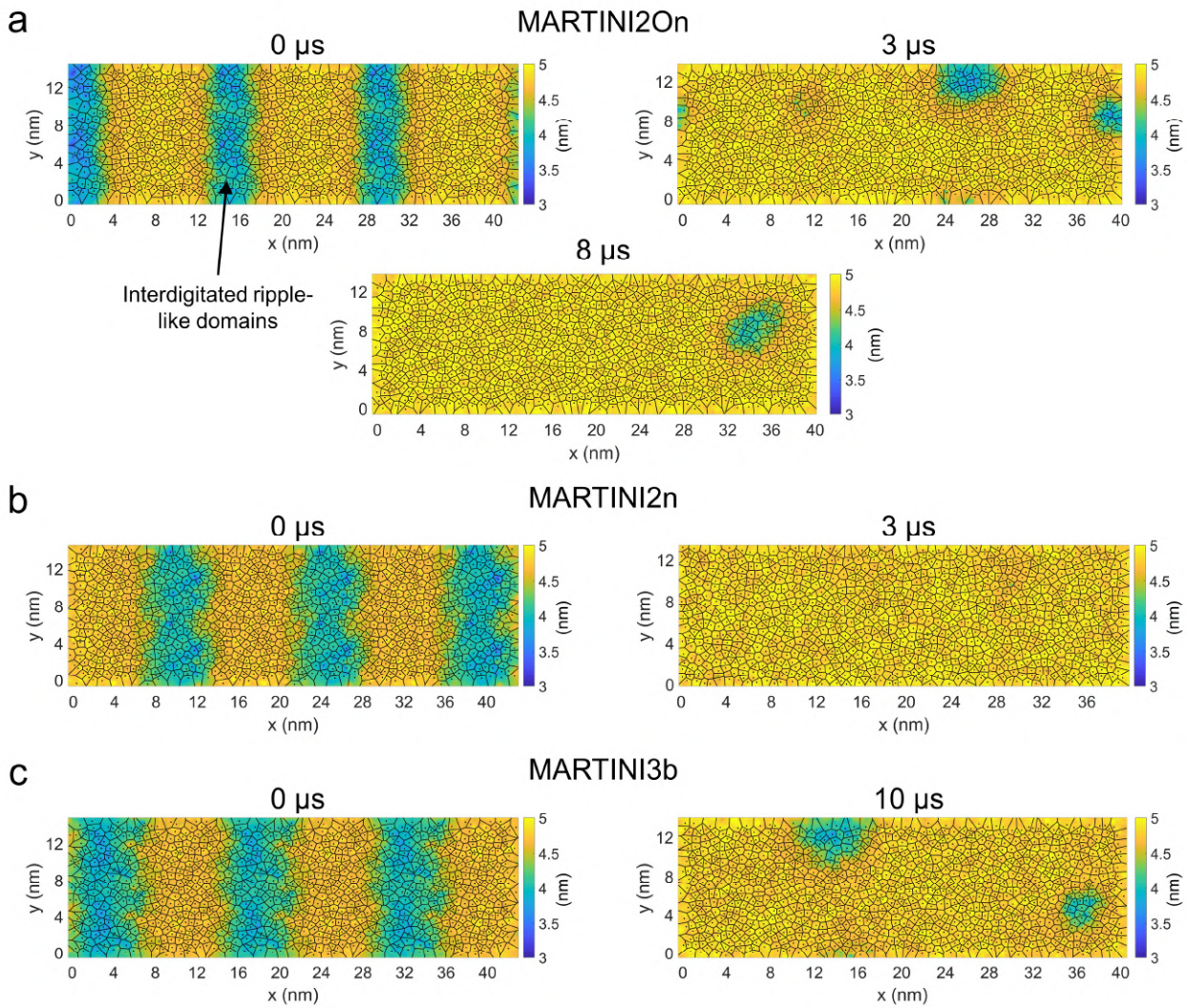

Fig. S10. Voronoi-thickness maps from MD of large MARTINI membranes. Voronoi-thickness map from constant temperature MD of large **(a)** MARTINI2On, **(b)** MARTINI2n, and **(c)** MARTINI3b membranes at 280 K, corresponding to MD snapshots in Fig. 5. Simulations starting with a periodic ripple-like configuration (0 μs), shows progressive loss of the interdigitated ripple-like domains and formation of the gel phase by 8 μs and 10 8 μs for the MARTINI2On and MARTINI3b membranes, respectively. Notably, the MARTINI2n membrane shows complete loss of interdigitation by 3 μs. Note that while the blue regions at the initial time points (0 μs) correspond to interdigitated domains, they could correspond to either interdigitated, or non-interdigitated but partially melted domains, at the final time points. The distinction can be made by simultaneously comparing the MD snapshots (Fig. 5) with the Voronoi-thickness maps above.

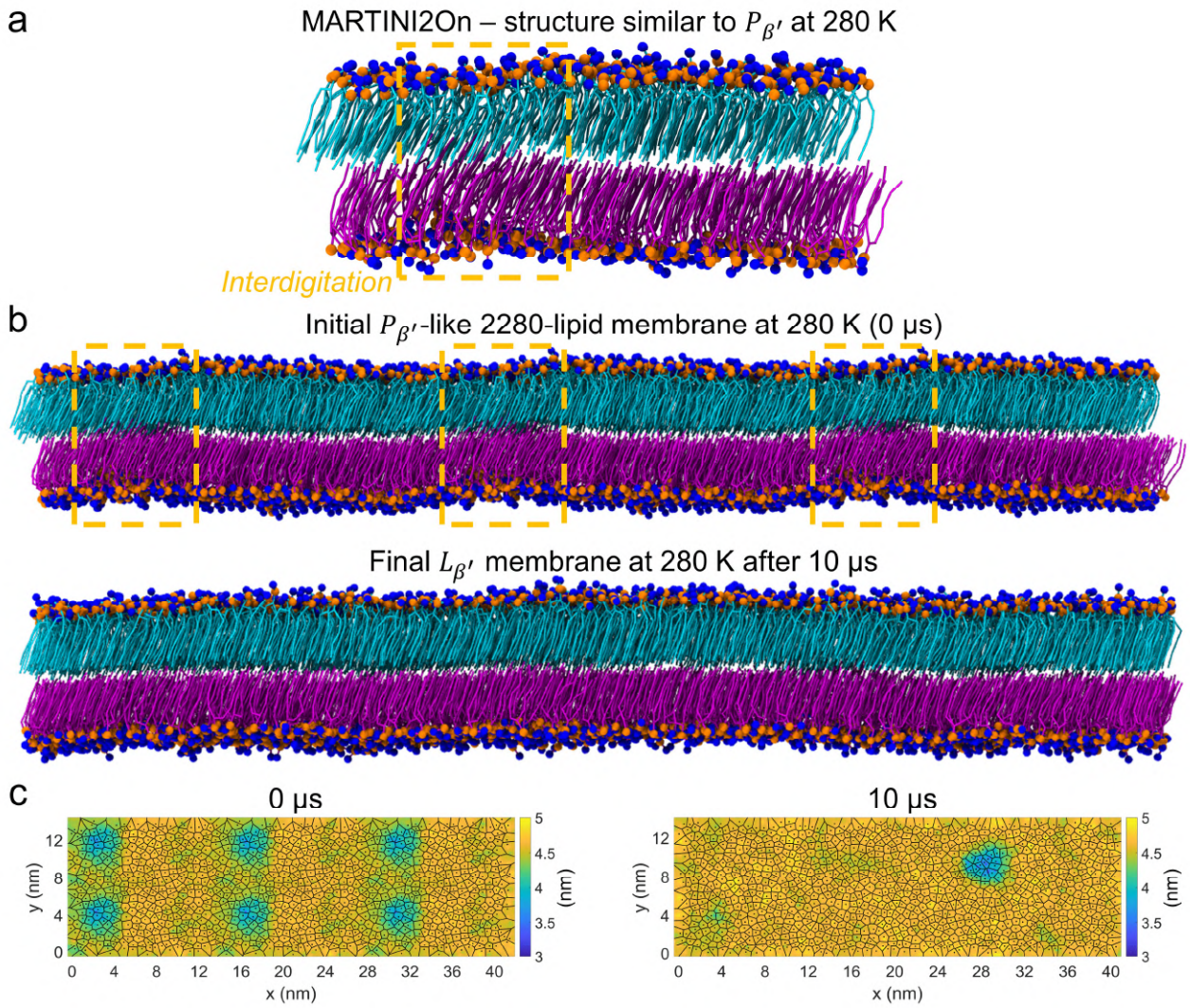

Fig. S11. Tilted ripple-like state of MARTINI2On membranes is also a finite size artefact. Simulated cooling of replicate 3 with the MARTINI2On FF (from Fig. S3) showed the formation of an interdigitated domain in an otherwise $L_{\beta'}$ membrane at 280 K. This structure was enhanced upon performing constant temperature MD for 5000 ns: final snapshot shown in **(a)**. **(b)** To explore whether this was a finite size effect or a true ripple phase, the smaller membrane was replicated 6x across periodic boundaries to create a larger membrane with repeated ripple-like domains (snapshot at 0 μs), similar to Fig. 5*a*. After 10 μs constant temperature MD, the interdigitated ripple-like regions were greatly diminished, thus confirming that the ripple-like state in (a) was indeed a finite size artefact. **(c)** Voronoi-thickness maps pertaining to MD snapshots in (b), where regions of lower thickness in blue indicate the ripple-like domains.